Cell Metabolism

Article

Lipid droplet-induced T cell death sustains autoimmune tissue inflammation

Graphical abstract

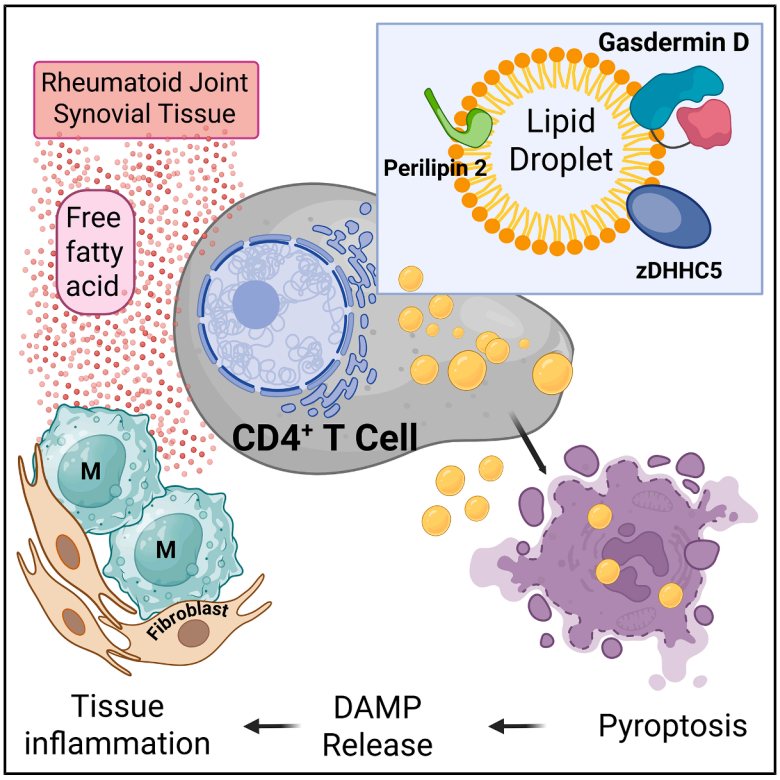

Highlights

- In RA, the tissue metabolic environment reprograms CD4⁺ T cells
- Lipid droplets in RA CD4⁺ T cells sequester gasdermin D and its activator zDHHC5
- RA lipid droplets act as killer organelles that induce pyroptotic membrane lysis
- Dying T cells expel intracellular contents that drive autoimmune tissue inflammation

Authors

Jitendra Kumar, Yoshinori Takashima, Jose Morales, ..., Gerald J. Berry, Jörg J. Goronzy, Cornelia M. Weyand

Correspondence

cweyand@stanford.edu

In brief

Kumar et al. identify a metabolically controlled trait of CD4⁺ T cells in autoimmune disease. Exposed to fatty acids in rheumatoid joints, they form lipid droplets containing pore-forming gasdermin D and its activator zDHHC5. These droplets induce plasma membrane lysis, resulting in the leakage of intracellular contents and tissue inflammation.

Kumar et al., 2026, Cell Metabolism *38*, 1–18
April 7, 2026
https://doi.org/10.1016/j.cmet.2026.01.014

CellPress

Please cite this article in press as: Kumar et al., Lipid droplet-induced T cell death sustains autoimmune tissue inflammation, Cell Metabolism (2026), https://doi.org/10.1016/j.cmet.2026.01.014

Cell Metabolism

CellPress
OPEN ACCESS

Article

Lipid droplet-induced T cell death sustains autoimmune tissue inflammation

Jitendra Kumar,[1,2,3] Yoshinori Takashima,[1,2,3] Jose Morales,[1,2,3] Brandon Wong,[1,2,3] Lina Werner,[1,2,3] Isabel N. Goronzy,[4,5] Selene Rubino,[1,2] Robert T. Trousdale,[6] Gerald J. Berry,[7] Jörg J. Goronzy,[1,2,8] and Cornelia M. Weyand[1,2,3,8,9,*]

[1]Department of Medicine, Mayo Clinic Alix School of Medicine, Rochester, MN 55905, USA
[2]Department of Immunology, Mayo Clinic College of Medicine and Science, Rochester, MN 55905, USA
[3]Department of Cardiovascular Medicine, Mayo Clinic Alix School of Medicine, Rochester, MN 55905, USA
[4]Division of Biology and Bioengineering, California Institute of Technology, Pasadena, CA, USA
[5]Yale School of Medicine, New Haven, CT, USA
[6]Department of Orthopedic Surgery, Mayo Clinic College of Medicine and Science, Rochester, MN 55905, USA
[7]Department of Pathology, Stanford University School of Medicine, Stanford, CA 94305, USA
[8]Department of Medicine, Stanford University School of Medicine, Stanford, CA 94305, USA
[9]Lead contact
*Correspondence: cweyand@stanford.edu
https://doi.org/10.1016/j.cmet.2026.01.014

SUMMARY

Autoimmunity leading to rheumatoid arthritis (RA) involves CD4$^+$ T cell recruitment into synovial tissue. However, metabolic conditions supporting the survival and pro-inflammatory effector functions of these tissue-invading T cells remain poorly understood. Lipidomic analysis identified the inflamed synovium as a lipid-rich environment. In functional studies, administration of the free fatty acid oleic acid exacerbated synovitis. Tissue-invading CD4$^+$ T cells responded to fatty acid with rapid cell lysis, releasing cytoplasmic and nuclear content into the extracellular space. This T cell lytic death required sequestration of the pore-forming molecule gasdermin D and the acyltransferase zDHHC5 to lipid droplets, which translocated to the plasma membrane to trigger membrane rupture and pyroptotic cell death. Targeting lipid droplet formation in CD4$^+$ T cells through perilipin-2 knockdown or inhibiting gasdermin activation by blocking protein acylation proved highly effective in suppressing synovitis. Thus, autoimmune CD4$^+$ T cells lack metabolic resilience, are primed to undergo pyroptosis in lipid-rich environments, and deliver pro-inflammatory cargo to surrounding tissue.

INTRODUCTION

Throughout a person's lifetime, approximately 10% of the population is diagnosed with a clinically significant autoimmune disease,[1] with no curative interventions currently available to restore immune tolerance. Chronicity of tissue inflammation presents a major challenge, and recent data have begun to illuminate antigen-independent factors, such as the metabolic restructuring of key effector cells that sustain inflammatory responses.[2] In CD4$^+$ T cells from patients with rheumatoid arthritis (RA), defective nuclear and mitochondrial DNA repair leads to metabolic deficiencies,[3] lysosomal underperformance,[4,5] and endoplasmic reticulum (ER) stress, transforming them into pro-inflammatory and tissue-damaging effector cells.[6] The impact of these bioenergetic deficiencies on T cell longevity and function within the tissue environment remains unclear.

Inflammation-promoting CD4$^+$ T cells must invade tissue spaces, survive, and interact with immune and stromal cells. The tissue-resident CD4$^+$ T cells found in the rheumatoid joint are predominantly central memory and effector memory cells,[4,7] while naive CD4$^+$ T cells are retained in lymph nodes, where they initially encounter antigens. Central memory and effector memory T cells are high-turnover populations, exhibiting average intermitotic (doubling) times of 15 and 48 days, respectively,[8] imposing significant proliferative stress and high bioenergetic and biosynthetic demands.

The synovial tissue is a glucose-starved enviroment,[9] favoring survival of glucose-independent cells. Thus, it provides a haven for CD4$^+$ T cells with downregulated extramitochondrial glycolysis[10] and limited capacity for mitochondrial ATP production.[11,12] Synovial tissue macrophages sustain their functions by accessing amino acids like glutamine and glutamate.[5,13] In RA CD4$^+$ T cells, glutamine anaplerosis is compromised due to *SUCLG1* downregulation and reversal of the tricarboxylic acid (TCA) cycle.[14] Consequently, mitochondrially impaired RA CD4$^+$ T cells accumulate intracellular acetyl-coenzyme A (CoA),[15] raising the critical question of how they manage extracellular and intracellular lipids. In the case of tumor-infiltrating CD8$^+$ T cells, upregulation of acetyl-CoA carboxylase and insufficient lipid catabolism threaten their survival and functional competence.[16]

Please cite this article in press as: Kumar et al., Lipid droplet-induced T cell death sustains autoimmune tissue inflammation, Cell Metabolism (2026), https://doi.org/10.1016/j.cmet.2026.01.014

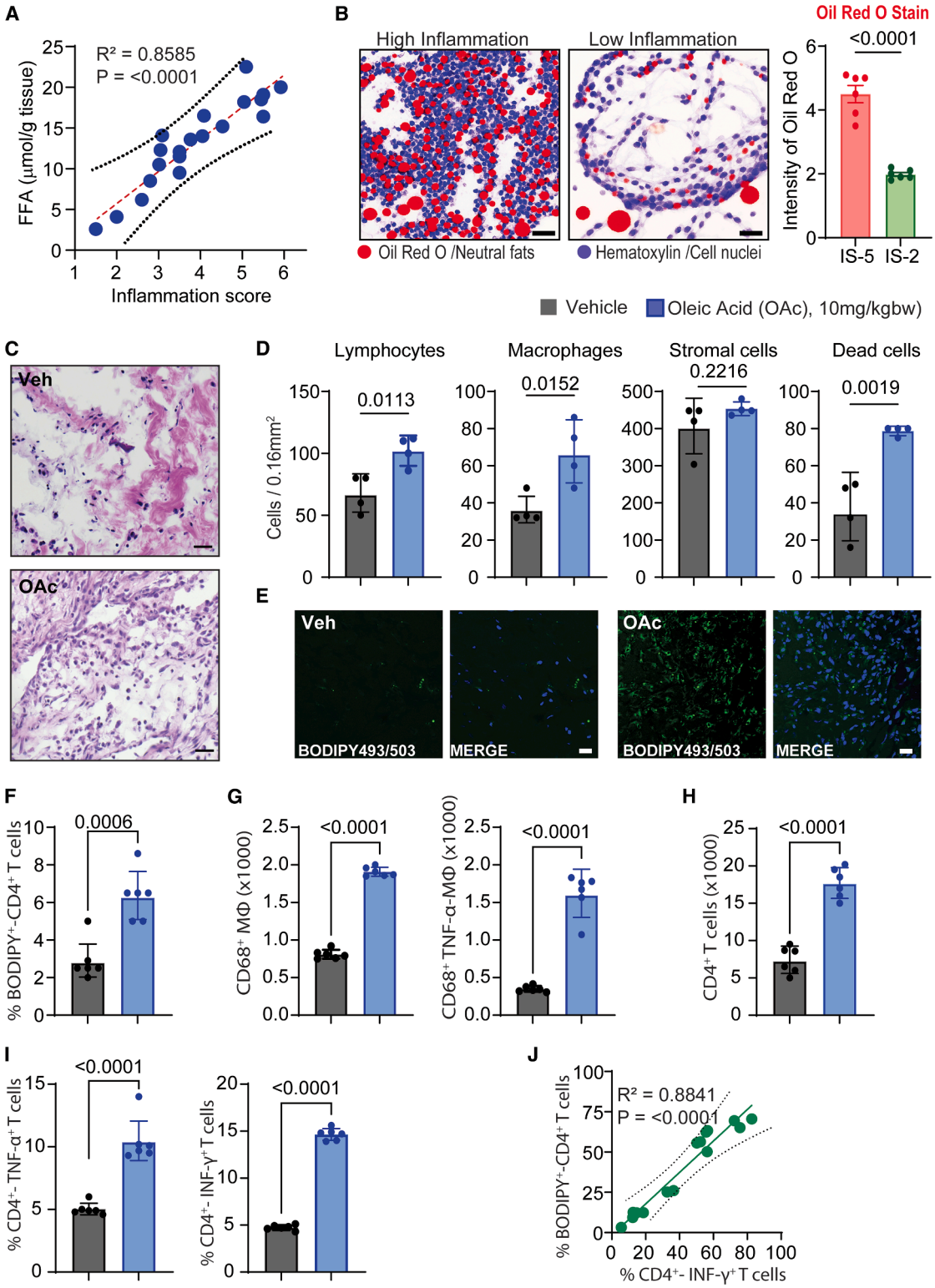

Figure 1. FFAs are deposited in the rheumatoid joint and exacerbate synovial tissue inflammation

(A) Correlation of FFA concentrations and inflammation scores (ISs) in rheumatoid synovium (n = 20).

(B) RA synovial tissue sections were stained with oil red O. Intensities were quantified in tissues with low and high ISs (n = 6 each).

(C–J) NSG mice engrafted with human synovium were immuno-reconstituted with human PBMCs. Chimeric mice were treated with vehicle or OAc (10 mg/kg) for 1 week. Explanted synovial tissues were processed for histology, immunofluorescence, and flow cytometry.

(legend continued on next page)

Please cite this article in press as: Kumar et al., Lipid droplet-induced T cell death sustains autoimmune tissue inflammation, Cell Metabolism (2026), https://doi.org/10.1016/j.cmet.2026.01.014

To mitigate lipid toxicity, cells store neutral lipids such as triglycerides and cholesterol esters in lipid droplets (LDs). Once thought to be mere fat storage sites, LDs are now recognized as dynamic cytoplasmic organelles that play crucial roles in lipid metabolism and cellular energy homeostasis.[17–20] LD proteomes are highly dynamic, with proteins involved in metabolism, signaling, and stress responses being recruited to or excluded from LD surfaces.[21,22] Highly mobile and capable of interacting with nearly every organelle, LDs act as portable signaling hubs, pivotal for maintaining cellular bioenergetics and providing buffering capacity during cellular stress responses.[17] In myeloid cells, LDs respond to danger-associated signals and serve as platforms for assembling inflammasome components.[23–26]

In this study, we have identified T cell lipid processing as a critical mechanism in sustaining chronic inflammation. Our findings demonstrate that the tissue exerts metabolic control over infiltrating T cells, transforming them into pro-inflammatory effector cells. Quantification of free fatty acids (FFAs) revealed that inflamed synovial tissue constitutes a lipid-rich environment, and treatment of humanized mice with oleic acid (OAc) identified FFAs as inflammatory accelerators. RA $CD4^+$ T cells, unable to metabolize lipids, arrived at this FFA-rich tissue site already filled with LDs. Mitochondrial impairment of RA $CD4^+$ T cells caused the translocation of two plasma membrane (PM) proteins to the LD surface: the pore-forming molecule GSDMD and the S-acyl transferase zDHHC5. Lipid stress initiated the rapid relocation of $GSDMD^+$-$zDHHC5^+$ LDs to the PM, triggering highly inflammatory pyroptotic cell death. Disrupting LD formation through perilipin-2 knockdown (KD) or inhibiting protein S-acylation effectively protects the tissue from inflammatory damage. Together, these findings elucidate a molecular mechanism by which the tissue microenvironment and LDs amplify inflammation: metabolically exhausted $CD4^+$ T cells are unable to withstand the lipid-rich environment and undergo pyroptosis. LDs loaded with GSDMD and its lipidating enzyme zDHHC5 transform such metabolically stressed $CD4^+$ T cells into drivers of chronic inflammation.

RESULTS

FFAs deposited in the rheumatoid joint exacerbate synovial inflammation

The synovial joint is a glucose-depleted and glutamine-rich environment,[9] requiring metabolic adaptations of invading immune cells. $CD4^+$ T cells account for ~30% of synovium-resident cells[27,28] and have a signature metabolic exhaustion,[4,13] including low mitochondrial output; low glycolytic activity, shunting toward the pentose phosphate pathway; and limited utilization of amino acids, such as glutamine.[4] To define bioenergetic resources for tissue-infiltrating $CD4^+$ T cells, we quantified FFAs in freshly collected synovial biopsies (Figure 1A). Tissue FFA concentrations were about 100-fold higher than steady-state plasma levels in humans. Notably, tissue inflammation scores were closely correlated with increasing FFA concentrations. Oil red O staining revealed diffuse deposition of neutral lipids, occupying the extracellular space between cells. Neutral lipid staining intensities correlated closely with tissue inflammation (Figure 1B).

Synovial FFA enrichment raised the question of whether lipids possess pro-inflammatory functions. We investigated the impact of FFA on disease activity in a human synovium-NSG mouse model. NSG mice were engrafted with human synovial tissues and reconstituted with patient-derived peripheral blood mononuclear cells (PBMCs). Chimeras were treated with intraperitoneal injections of OAc (10 mg/kg) for 1 week (Figure S1A). We chose OAc as a representative monounsaturated omega-9 fatty acid (18:1 *cis*-9) that is enriched in RA synovial tissue.[29,30] OAc treatment markedly exacerbated synovial tissue inflammation (Figure 1C). OAc-treated grafts were densely infiltrated by lymphocytes and macrophages, accrued dead cells, and lipid deposits (Figures 1C–1E). OAc treatment caused LD accumulation within tissue-infiltrating $CD4^+$ T cells (Figure 1F), and enhanced cytokine production by tissue macrophages and $CD4^+$ T cells (Figures 1G–1I). Frequencies of interferon (IFN)-γ^+CD4^+ T cells correlated with LD formation and cell death rates (Figures 1J and S1B), linking lipid-induced inflammation to cellular death.

Together, these data identify FFA as inflammatory stimuli, activating both tissue T cells and macrophages and inducing cell death.

RA $CD4^+$ T cells are loaded with intracellular LDs rich in OAc

Having identified FFA deposits as a feature of the inflamed joint, we aimed to investigate how such FFAs affect the survival and function of tissue-infiltrating $CD4^+$ T cells. We analyzed intracellular FFA and LD accumulation as a proxy for intracellular FFA storage. Patients with psoriatic arthritis (PsA) served as inflammatory disease controls. Compared with controls, RA $CD4^+$ T cells had ~40% more intracellular FFAs (Figure 2A). We isolated LDs from $CD4^+$ T cells and performed lipidomic analysis to compare the FFA distribution in RA and healthy LDs. Two FFAs, OAc and myristic acid, were significantly enriched in RA LDs, suggesting that RA $CD4^+$ T cells have access to

(C) Representative synovial tissue sections (H&E).
(D) Histomorphometric analysis of tissue sections to quantify frequencies of lymphocytes, macrophages, stromal cells, and dead cells.
(E) Synovial tissue sections were stained with BOPIDY493/503, and nuclei were marked with DAPI.
(F–I) Tissue-infiltrating cells in vehicle vs. OAc-treated grafts quantified by flow cytometry.
(F) Frequencies of $BODIPY493/503^+CD4^+$ T cells.
(G) Frequencies of $CD68^+$ macrophages and TNF-producing $CD68^+$ macrophages.
(H) Frequencies of tissue-infiltrating $CD4^+$ T cells.
(I) Frequencies of TNF-α- and IFN-γ-producing $CD4^+$ T cells.
(J) Correlation between frequencies of $BODIPY493/503^+$ and IFN-producing $CD4^+$ T cells.
All data are mean ± SEM with individual values shown. Unpaired Mann-Whitney-Wilcoxon rank test (B, D, and F–I). Spearman correlation coefficient (A and J). Scale bar, 50 μm.

Please cite this article in press as: Kumar et al., Lipid droplet-induced T cell death sustains autoimmune tissue inflammation, Cell Metabolism (2026), https://doi.org/10.1016/j.cmet.2026.01.014

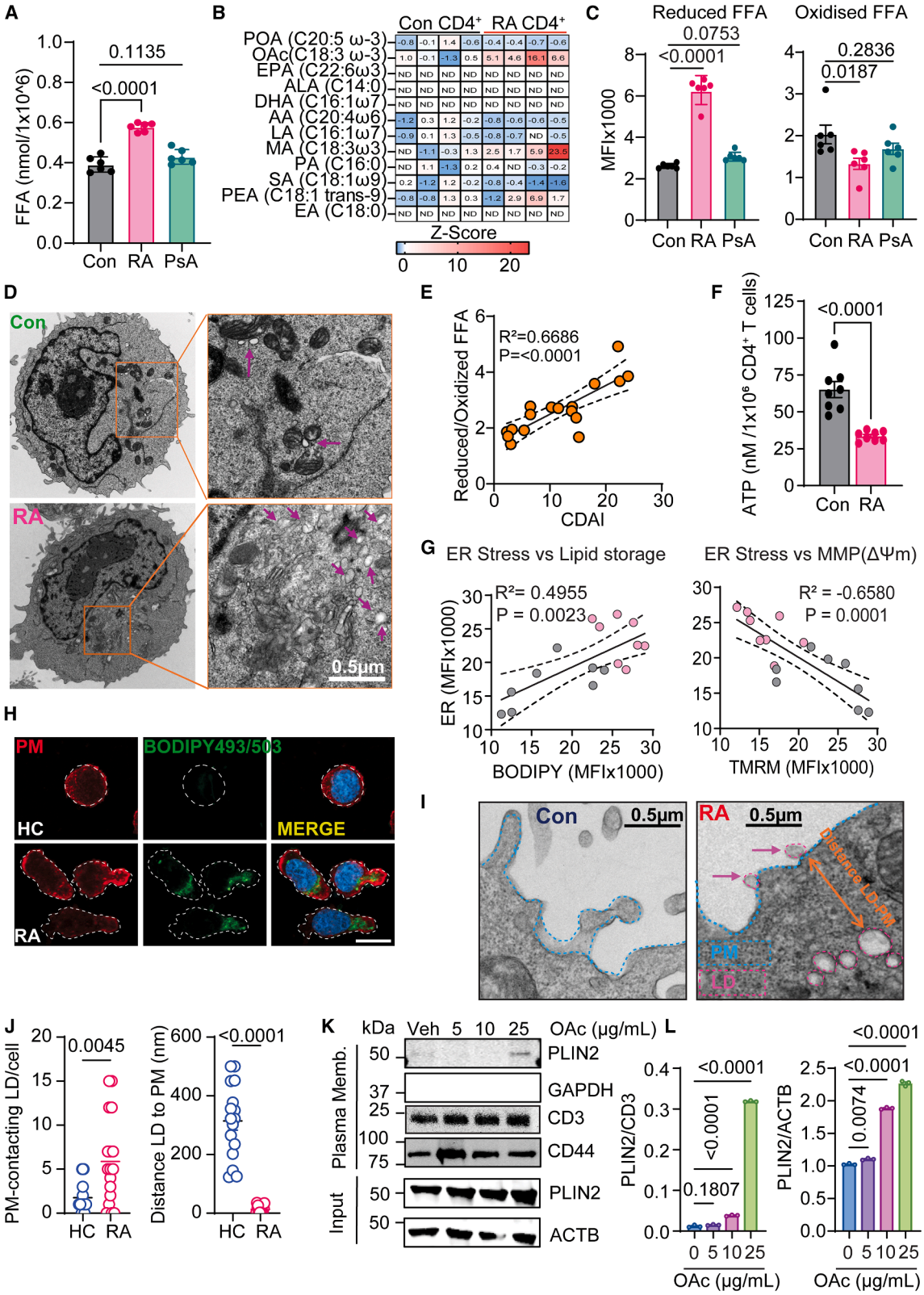

Figure 2. Metabolically exhausted CD4⁺ T cells accrue intracellular lipids

Peripheral blood CD4⁺CD45RO⁻ T cells isolated from healthy controls, patients with RA, or patients with PsA were stimulated for 72 h.

(A) FFAs were quantified in CD4⁺ T cell lysates (n = 6/group).

(legend continued on next page)

Please cite this article in press as: Kumar et al., Lipid droplet-induced T cell death sustains autoimmune tissue inflammation, Cell Metabolism (2026), https://doi.org/10.1016/j.cmet.2026.01.014

OAc-enriched lipid stores (Figure 2B). Notably, patient-derived CD4$^+$ T cells accumulated reduced but not oxidized FFAs (Figure 2C). Transmission electron microscopy visualized dense LD clusters almost exclusively in RA CD4$^+$ T cells (Figure 2D). In a cross-sectional cohort of 17 patients with RA, the reduced/oxidized FFA ratio was closely correlated with the clinical disease activity index (CDAI) (Figure 2E). Consistently, highly active RA was associated with the accrual of un-oxidized fatty acids in CD4$^+$ T cells (Figures S2A and S2B).

Given the unexpected finding that production and storage of reduced intracellular lipids distinguished RA and healthy CD4$^+$ T cells, we focused on the metabolic competence of RA T cells.[13] Gene expression profiling demonstrated a bias toward lipogenesis in RA CD4$^+$ T cells and upregulation of CD36, while other fatty acid transporters were unchanged (Figure S2C). RA CD4$^+$ T cells responded to stimulation with low ATP production, confirming our prior data of mitochondrial deficiency.[15] Additionally, RA CD4$^+$ T cells accumulated acetyl-CoA and citrate (Figures 2F, S2D, and S2E), compatible with a defect in lipid catabolism. LDs are born in the ER, prompting us to assess ER size and ER stress markers. Higher BODIPY493/503 signal was associated with larger ER size in individual CD4$^+$ T cells (Figure 2G). Correlation analysis revealed a significant inverse relationship between ER size (ER-Tracker) and mitochondrial fitness (mitochondrial membrane potential; TMRM or mitoROS) (Figures 2G and S2F). ER size expansion in RA CD4$^+$ T cells was associated with the upregulation of canonical ER stress markers (Figure S2G). Co-localization studies placed LDs closely to mitochondria in healthy CD4$^+$ T cells and geographically separated in RA CD4$^+$ T cells (Figure S3A). Uropodal accumulation of LDs, distant from perinuclear mitochondria, strongly suggested that RA CD4$^+$ T cells failed to catabolize FFAs and instead allocated them to storage. Accordingly, inhibiting mitochondrial ATP synthase with oligomycin was sufficient to expand ER membranes (Figure S3B) and thus LD biogenesis, linking inappropriate T cell lipid cargo to mitochondrial failure.

Placing LD formation into the context of interorganelle communication prompted us to define the subcellular distribution of LDs and map contact points between LDs and other cellular compartments. Multiparametric immunofluorescence staining placed the LDs into the T cell uropod, a migration-enabling cell protrusion typical of activated and polarized T cells (Figure 2H). RA CD4$^+$ T cells frequently formed a uropod (Figure S3C), in line with their hypermobile state.[12] LDs were almost exclusively localized near the uropodal PM. LD-PM distances were 300–400 nm in healthy cells but shrank to <20 nm in RA CD4$^+$ T cells (Figures 2I and 2J). Often, LDs aligned like a "string of pearls" along the inner and outer PM face. Lipid stress, imposed by treating CD4$^+$ T cells with exogenous OAc, rapidly moved LDs to the PM and induced integration of PLIN2 into the membrane. We confirmed direct LD-PM contact by isolating cell membranes of lipid-stressed CD4$^+$ T cells (marker molecules CD3 and CD44) and probing with anti-PLIN2 antibodies to demonstrate incorporation of the LD protein into the PM (Figures 2K and 2L).

Together, these data suggest that mitochondrial deficiency in RA CD4$^+$ T cells restructures subcellular organelles (ER membrane extension, LD formation) and redistributes LDs toward the PM.

FFA-rich tissues are detrimental to metabolically exhausted T cells

Prompted by data demonstrating FFA enrichment in both the inflamed synovial tissue and tissue-resident CD4$^+$ T cells, we examined how FFAs regulate T cell survival and function and whether they shift T cells toward pathogenic effector functions. We collected CD4$^+$ T cells from the peripheral blood of healthy controls and patients with RA and the synovial tissue of patients with RA. We exposed all CD4$^+$ T cells to lipid stress, tracked their response using live-cell imaging, and quantified cell death (Figures 3A and 3B). Given the enrichment of OAc in RA LDs, we treated T cells with OAc. Healthy CD4$^+$ T cells contained few LDs and survived the lipid challenge (Figure 3C). Circulating RA CD4$^+$ T cells carried small LDs and were predisposed to death. OAc treatment induced PM disintegration and accelerated death rates. CD4$^+$ T cells from RA tissue were packed with large, confluent LDs and were highly susceptible to lipid stress, with only a fraction still alive after 1 h (Figures 3C and 3D). Lipid-exposed cells underwent cellular swelling (Figures 3E and 3F) and complete PM fragmentation (Figure S4A).

(B) LDs were isolated from control and RA CD4$^+$ T cells, and FFAs were quantified by liquid chromatography-tandem mass spectrometry (LC-MS/MS). Data are shown as a *Z* score heatmap, with values normalized to the internal standard (n = 4/group).
(C) CD4$^+$ T cells were stained with BODIPY581/591-C11, and reduced and oxidized FFAs were measured by flow cytometry. Mean fluorescence intensities (MFIs) from n = 6/group are shown.
(D) Representative electron microscopy images from healthy and RA CD4$^+$ T cells. Purple arrows indicate LDs. 30 cells were examined from each of 3 controls and 3 RA patients. Scale bar, 0.5 μm.
(E) Ratios of reduced/oxidized FFAs in CD4$^+$ T cells were correlated with the CDAI in 17 patients.
(F) Intracellular ATP was quantified in control and RA CD4$^+$ T cells (n = 6 each).
(G) CD4$^+$ T cells from healthy controls (n = 8) and RA (n = 8) were stained with BODIPY493/503, TMRM, and ER-Tracker. Correlations of ER size (ER-Tracker) vs. intracellular lipids (BODIPY493/503) and ER-Tracker vs. TMRM are shown. Gray dots, healthy controls. Pink dots, RA.
(H) Representative immunofluorescence images showing LD accumulation in the uropod of RA CD4$^+$ T cells. PMs (wheat germ agglutinin [WGA], red), LDs (BODIPY493/503, green), and nuclei (DAPI, blue). White dashed lines mark cell perimeters (n = 6/group). Scale bar, 5 μm.
(I) Representative electron microscopy images from control and RA CD4$^+$ T cells (n = 3 each). Purple arrows mark LDs, blue dashed lines show PM, and orange arrows indicate the LD-to-PM distance. Scale bar, 0.5 μm.
(J) Enumeration of LDs in direct contact with the PM (left) and LD-to-PM distances (right); 50 cells/sample.
(K and L) Lipid-induced integration of PLIN2 into the PM. CD4$^+$ T cells were treated with increasing doses of OAc; PMs were isolated and immunoblotted for PLIN2, CD3, CD44, GAPDH, and β-actin. Bar graphs show PLIN2 quantification normalized to CD3 and β-actin, respectively. Data from three experiments.
All data are mean ± SEM with individual data points shown. One-way ANOVA with Dunnett's multiple comparisons test (A–C and L). Spearman correlation coefficient (E and G). Unpaired Mann-Whitney-Wilcoxon rank test (F and J).

Please cite this article in press as: Kumar et al., Lipid droplet-induced T cell death sustains autoimmune tissue inflammation, Cell Metabolism (2026), https://doi.org/10.1016/j.cmet.2026.01.014

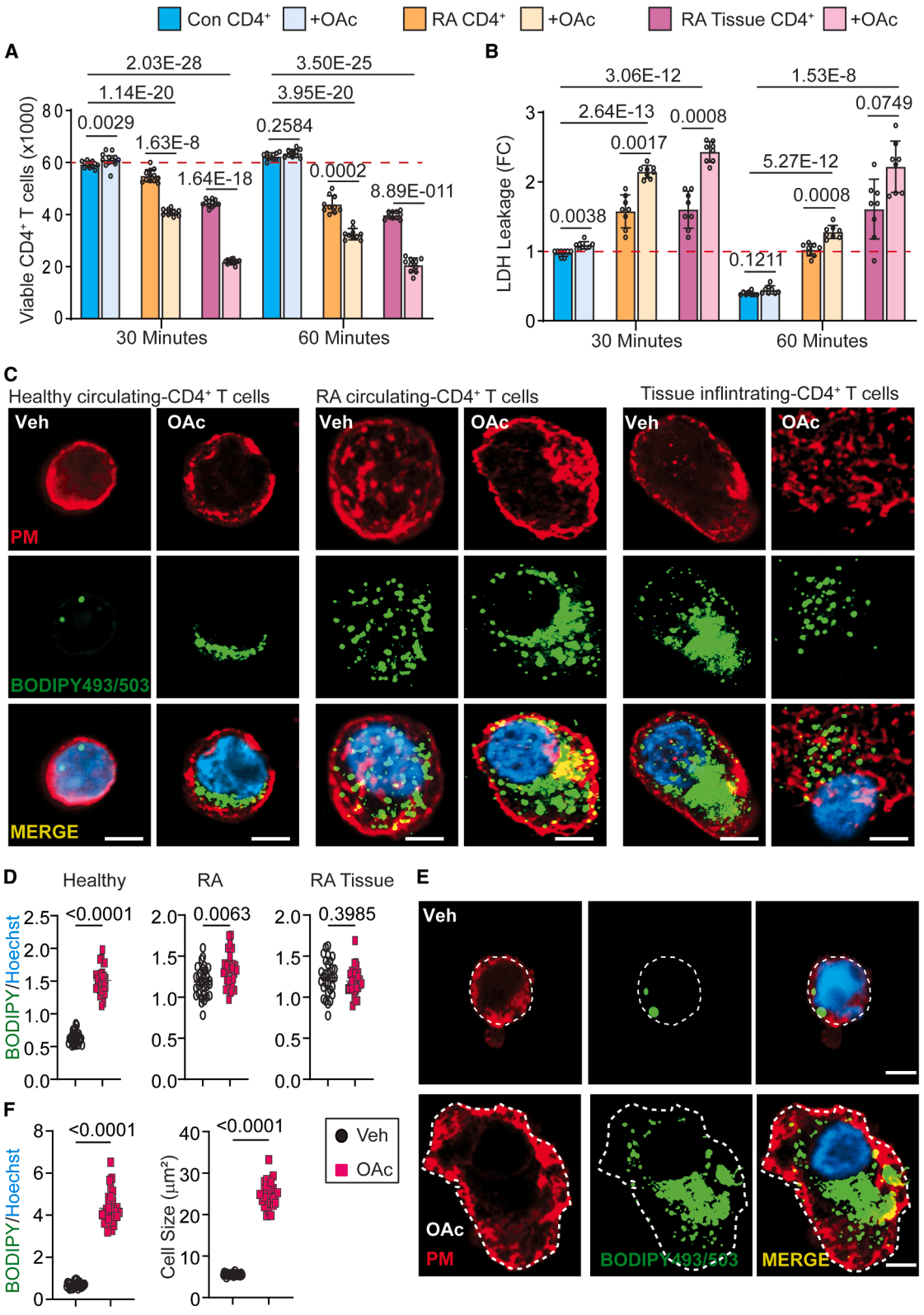

Figure 3. Fatty acids induce PM damage in CD4+ T cells

Peripheral blood CD4+CD45RO- T cells from controls and RA patients were stimulated for 72 h. Tissue CD4+ T cells were derived from digested RA synovial tissue biopsies. T cells were treated with vehicle or OAc (10 μg/mL) for 30 and 60 min.

(legend continued on next page)

Please cite this article in press as: Kumar et al., Lipid droplet-induced T cell death sustains autoimmune tissue inflammation, Cell Metabolism (2026), https://doi.org/10.1016/j.cmet.2026.01.014

Imaging studies suggested that LDs were integrated into the PM before being expelled into the extracellular space (Figure 3E). T cell death induction was dose dependent (Figure S4B).

These results support the concept that LD-bearing CD4$^+$ T cells are at risk for membrane pore formation and cell death, enabling FFA-rich tissues to transform invading T cells into inflammation inducers.

RA CD4$^+$ T cells sequester the pore-forming molecule GSDMD in LD

LD ejection from the T cell uropod and membrane disintegration elicited by exogenous lipids pointed to the possibility of LDs inducing lytic cell death. We isolated LDs from control and RA CD4$^+$ T cells and proceeded with mass spectrometry-based proteomics (Figures S5A and S5B). LDs derived from control, fatty acid-loaded control, and RA CD4$^+$ T cells displayed distinguishing protein profiles, with RA disease state and lipid loading resulting in coordinated upregulation of proteins (Figures 4A and 4B; Table S1). LDs from RA and fatty acid-stressed T cells shared the enrichment of proteins involved in LD structural support, fatty acid metabolism, and lipid transport (PLIN2, FASN, and PGRMC1). A group of enriched proteins (ECI1, DECR1, CLUH, and HADHA/HADHB) typically associated with LD-mitochondria contact sites indicated high mitochondrial stress in both RA- and FFA-exposed T cells. Accumulation of the palmitoyl-protein hydrolase LYPLA2 pointed toward possible LD engagement in membrane lipid modifications. Finally, the increased representation of GSDMD and its activating protease, caspase-1 (CASP1)—both key mediators of inflammasome-induced membrane pore formation—suggested a potential crosstalk between lipid metabolism and inflammatory cell-death pathways. Table S1 Pathway enrichment analysis of RA LD-enriched proteins yielded a strong association with fatty acid metabolism, inflammasome activity, oxidative stress, mTORC1 signaling, and exosomal pathways (Figure S5C).

The structural protein PLIN2 is embedded into the LD membrane and protects LDs from autophagy.[31] We confirmed that high expression of PLIN2 distinguished RA CD4$^+$ T cells from healthy and disease-control T cells (Figures 4C–4E and S5D). *PLIN2* mRNA quantification in CD4$^+$ T cells from patients with four autoimmune diseases (RA, PsA, systemic lupus erythematosus [SLE], and granulomatosis with polyangiitis [GPA]) excluded systemic inflammation as the sole driver of *PLIN2* upregulation (Figure 4F). In RA CD4$^+$ T cells, *PLIN1* and *PLIN2* mRNA levels were spontaneously elevated (Figure S5E), compatible with a poised state for FFA accumulation and LD building.

To validate GSDMD's integration into LDs, we compared expression of PLIN2 and GSDMD in purified LDs. PLIN3 served as loading control.[32] Immunoblotting confirmed that RA LDs carried 2-fold higher amounts of PLIN2 and consistently contained GSDMD, while GSDMD was undetectable in healthy LDs (Figure 4G). Caspase (CASP)-dependent GSDMD cleavage releases an active GSDMD-N-terminal p30 fragment that oligomerizes and forms PM pores.[33] Transcriptomic analysis and immunoblotting documented spontaneous upregulation of GSDMD exclusively in RA CD4$^+$ T cells (Figures 4H and 4I). Immunofluorescence staining localized GSDMD to the uropod of RA CD4$^+$ T cells, where it co-localized with BODIPY$^+$ LD (Figure 4J). The protein remained undetectable in healthy CD4$^+$ T cells.

In essence, RA CD4$^+$ T cells are primed to form specialized LDs, which transport the pore-forming molecule GSDMD.

LD-rich CD4$^+$ T cells die by pyroptosis

Next, we examined whether GSDMD sequestration into the LD has a role in lipid-induced T cell death. GSDMD-dependent cell death requires cleavage of auto-inhibited GSDMD and generation of active N-terminal fragments, which oligomerize into large membrane pores.[34] Lipid-induced cell body swelling and release of intact LDs (Figure 3E) strongly suggested lytic death of RA CD4$^+$ T cells, instead of anti-inflammatory death.[35] Live-cell imaging of tissue-derived RA CD4$^+$ T cells showed ejection of intact nuclei (Figure 5A), a process aggravated by OAc. Supernatants from RA but not healthy CD4$^+$ T cells contained nuclear DNA and PLIN2 protein (Figures 5B and S6A). OAc-induced lipid stress imposed rapid PM disintegration in patient-derived T cells, which breached their cell membrane and became SYTOX positive (Figures 5C and 5D). Lipid treatment consistently increased lactate dehydrogenase (LDH) leakage and cell death (Figure S6B). Together, these morphologic changes support a lytic and an inflammatory cell death mode of LD-loaded T cells.

GSDMD cleavage requires activation of upstream sensors and CASPs. We pursued a molecular definition of lipid-induced cell death based on gene induction elicited by stressing CD4$^+$ T cells with OAc and palmitic acid (PA). CD4$^+$ T cells responded to both fatty acids by regulating a similar gene signature: *PLIN2*, *NLRP3*, *CASP1*, *GSDMD*, *IL-1b*, and *IL-18* (Figure 5E). Immunoblot analysis of cell supernatants detected the release of cleaved CASP1, interleukin (IL)-1β, and IL-18 in RA (Figure 5F) and lipid-stressed CD4$^+$ T cells (Figure 5G). Lipid treatment enhanced NLRP3, CASP1, and GSDMD protein expression, and cell lysates had a signal for GSDMD-N, all supporting pyroptosis as the relevant cell death (Figure 5G). Plasma samples from patients with RA contained elevated levels of IL-1β, compatible with continuous CASP1 activation (Figure S6C). Lack of CASP3/7/8 cleavage ruled out apoptosis and PANoptosis[36] (Figure S6D).

(A and B) Quantification of CD4$^+$ T cell survival after OAc treatment. Cell viability measured by trypan blue exclusion or LDH leakage. Dashed lines represent average control levels. Data from 8 to 12 experiments.
(C) Cellular response patterns to OAc treatment analyzed by confocal live-cell imaging. PMs (WGA, red); LDs (BODIPY493/503, green); nuclei (Hoechst-33342, blue) (n = 12/group). Scale bar, 5 μm.
(D) OAc-induced lipid loading quantified by BODIPY493/503 staining. 30 cells analyzed/sample (n = 6/group).
(E) Live-cell image of RA CD4$^+$ T cells treated with OAc (10 μg/mL) for 6 h. Dashed lines mark cell boundaries. Representative data from six experiments. Scale bar, 5 μm.
(F) Intensity of BODIPY493/503/Hoechst-33342 and cell sizes were calculated. 30 cells analyzed/sample (n = 6/group).
Mean ± SEM with individual data points shown. Control vs. treatment, paired Student's t test (A and B); control PBMC vs. RA PBMC and RA synovial tissue, unpaired Student's t test adjusted for multiple comparison using Holm-Šídák method (A and B). Unpaired Student's t test (D and F).

Please cite this article in press as: Kumar et al., Lipid droplet-induced T cell death sustains autoimmune tissue inflammation, Cell Metabolism (2026), https://doi.org/10.1016/j.cmet.2026.01.014

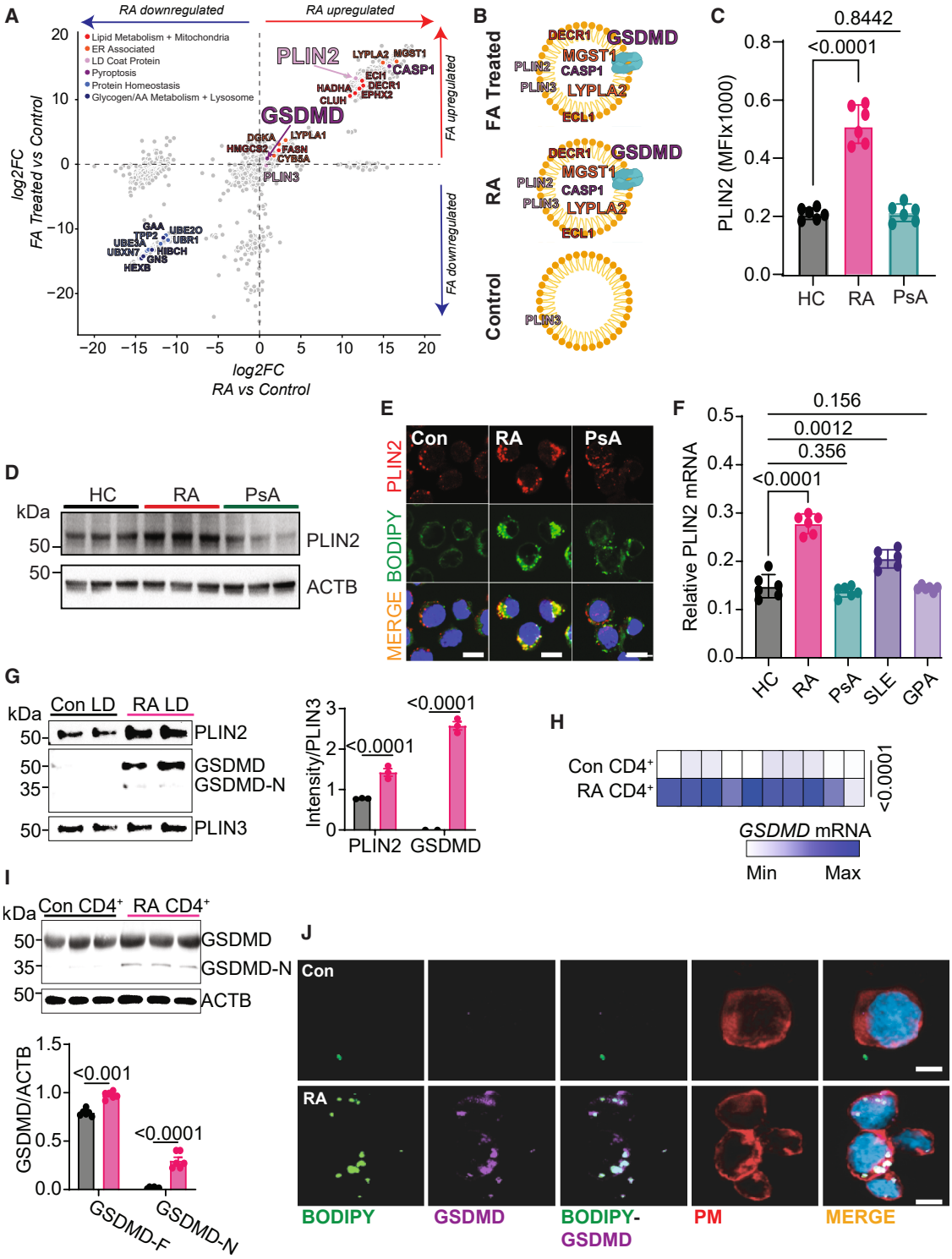

Figure 4. LDs in RA CD4⁺T cells sequester the pore-forming molecule GSDMD

CD4⁺CD45RO⁻ T cells from patients with RA or PsA and from age-matched controls were stimulated for 72 h.

(A) LDs isolated from control, fatty acid-treated CD4⁺ T cells, and RA CD4⁺ T cells (n = 3) were subjected to proteomics analysis. Scatterplot demonstrates log2 protein abundance fold change of RA versus control (x axis) versus log2 protein abundance fold change of FA-treated versus control (y axis). Vertical and horizontal dashed lines represent unchanged protein level (fold change equal to zero). Key molecules of interest are highlighted and labeled.

(B) Schematic of LDs in FA-treated (top), RA (middle), and control (bottom) CD4⁺ T cells.

(legend continued on next page)

Please cite this article in press as: Kumar et al., Lipid droplet-induced T cell death sustains autoimmune tissue inflammation, Cell Metabolism (2026), https://doi.org/10.1016/j.cmet.2026.01.014

Lipid stress did not upregulate ferroptosis-related genes (Figure S7A), in line with the accumulation of reduced but not oxidized FFA in RA CD4$^+$ T cells (Figure 2C). In support, pretreatment of RA CD4$^+$ T cells with the ferroptosis inhibitors ferrostatin-1 and liproxstatin-1 did not protect from lytic cell death (Figures S7B–S7E).

Accordingly, extracellular lipids emerge as inducers of pyroptosis, and RA CD4$^+$ T cells are primed to respond to FFA with pyroptotic cell death.

LDs in RA CD4$^+$ T cells absorb the acyltransferase zDHHC5

GSDMD sequestration into LDs shifted the function of these organelles from lipid storage vesicles to membrane pore inducers, provided that GSDMD is released from its self-inhibited state. Membrane pore formation involves CASP-dependent cleavage, liberation of GSDMD-N, and assembly into large transmembrane channels, achieved by partnering GSDMD with fatty acid synthase and acyltransferase-dependent S-acylation.[37,38] In RA CD4$^+$ T cells, GSDMD-loaded LDs redistributed to the inner PM face (Figures 2I and 2J) and formed direct contact points. To pursue the hypothesis that GSDMD could be activated within the LD, we identified relevant S-acylases and investigated whether specific members of the *zDHHC* family facilitated LD-induced membrane injury in T cells. In a focused expression screen of 22 *zDHHC* genes, *zDHHC5*, *zDHHC17*, and *zDHHC20* were significantly upregulated in RA T cells (Figure 6A). Previous reports have assigned zDHHC5 and zDHHC20 as primarily PM located,[39,40] identifying them as candidate PATs in GSDMD lipidation (Figure 6B). Silencing of *zDHHC5* or the *KD-zDHHC5/KD-zDHHC20* combination in lipid-stressed RA CD4$^+$ T cells significantly reduced SYTOX uptake and LDH leakage (Figures 6C–6E). *zDHHC5* KD attenuated the extracellular release of LDs and of nuclear DNA (Figures 6F and 6G). These data placed zDHHC5-mediated S-acylation upstream of LD-dependent membrane disintegration and the spread of inflammatory materials into the tissue space.

To understand GSDMD-zDHHC5 interactions in LD-dependent membrane damage, LD ejection, and DNA release, we mapped the subcellular positioning of the enzyme. Immunoblot analysis of the isolated LD and PM fractions verified the enrichment of zDHHC5 and PLIN2 in both the LD and the PM fractions (Figure 6H). RA CD4$^+$ T cells had a stronger signal for zDHHC5 than healthy T cells, with expression in both the PM and in LDs (Figure 6I). Also, pull-down experiments yielded support for PLIN2-zDHHC5 complex formation in LDs isolated from lipid-stressed RA CD4$^+$ T cells (Figure 6J).

Taken together, these findings identify zDHHC5 as a PLIN2 binding partner on the LD membrane coating and implicate the enzyme in GSDMD acylation and PM poration in lipid-stressed T cells.

Blocking lipidation in CD4$^+$ T cells protects tissue from inflammation

To explore the biological relevance of GSDMD lipidation, we examined whether blocking GSDMD acylation prevents tissue inflammation. 2-Bromopalmitate (2-BP) and cyano-myracrylamide (CMA)[42,43] are S-acylation pan-inhibitors that block zDHHC-dependent GSDMD modification.[34] Treatment with the pan-acylation inhibitors efficiently protected the membrane of lipid-stressed RA CD4$^+$ T cells from damage (Figures S8A and S8B). To validate the cytoprotective effect *in vivo*, we treated synovium-engrafted NSG mice with 2-BP or CMA (Figure S8C). Treatment markedly reduced synovial cell infiltration, dead cell accumulation, and macrophage and lymphocyte accumulation (Figures 7A and 7B). Blocking GSDMD acylation sharply suppressed the tissue recruitment of CD4$^+$ T cells and of IFN-γ- and tumor necrosis factor (TNF)-producing T cells. Restraining S-acylation diminished CD68$^+$ macrophage infiltration, including TNF- and IL-6-producing macrophages. Cytoprotective and anti-inflammatory effects of 2-BP and CMA extended to the synovial stromal cell population, where frequencies of pro-inflammatory IL-6$^+$FAP$^+$ fibroblast-like synoviocytes declined (Figure 7C). Inhibition of S-acylation effectively prevented LD deposition in the synovial tissue space (Figures 7D and 7E) and diminished levels of PLIN2 circulating in the plasma (Figure 7F).

These proof-of-principle treatment trials endorsed the concept that S-acylation is a critical checkpoint in LD biogenesis and LD-induced membrane damage, with zDHHC5 functioning as a key mediator of lipid-induced membrane poration.

LDs are pro-inflammatory organelles in rheumatoid synovitis

Above findings classified LDs as potentially inflammatory organelles, inflicting membrane damage and pyroptotic T cell death. We pursued the question of whether LDs per se represent therapeutic targets and whether the suppression of LD formation in CD4$^+$ T cells protects synovial tissue from inflammatory attack. To modulate LD abundance in T cells, we targeted PLIN2, a critical LD structural protein.[44]

We either increased or decreased *PLIN2* expression selectively in purified CD4$^+$ T cells, transferred them into tissue-engrafted NSG chimeras (Figures S9A and S9B), and then examined the intensity of synovial tissue inflammation. PLIN2

(C–E) Quantification of PLIN2 expression in CD4$^+$ T cells.
(C) Flow cytometric analysis of PLIN2 in CD4$^+$ T cells (n = 6/group).
(D) Representative immunoblot of PLIN2 in control, RA, and PsA CD4$^+$ T cells (n = 3/group).
(E) Representative immunofluorescence images of PLIN2 and BODIPY493/503 in control, RA, and PsA CD4$^+$ T cells. Scale bar, 10 μm (n = 6/group).
(F) *PLIN2* mRNA (RT-qPCR) in CD4$^+$ T cells from controls and patients with RA, PsA, SLE, and GPA (n = 6/group).
(G) Immunoblot of PLIN2 and GSDMD in control and RA LDs. Loading control, PLIN3. Bar graphs show band intensities.
(H) Heatmap of *GSDMD* mRNA transcript from control and RA (n = 10/group).
(I) Immunoblot of GSDMD-F and the active fragment GSDMD-N in control and RA CD4$^+$ T cells. Band intensities shown as bar graphs (n = 6/group).
(J) Representative images showing co-localization of GSDMD and LDs. Scale bar, 5 μm.
Data are mean ± SEM with individual data points shown. One-way ANOVA with Dunnett's multiple comparisons (C, F, and G). Multiple t tests with two-stage step-up (H and I).

Please cite this article in press as: Kumar et al., Lipid droplet-induced T cell death sustains autoimmune tissue inflammation, Cell Metabolism (2026), https://doi.org/10.1016/j.cmet.2026.01.014

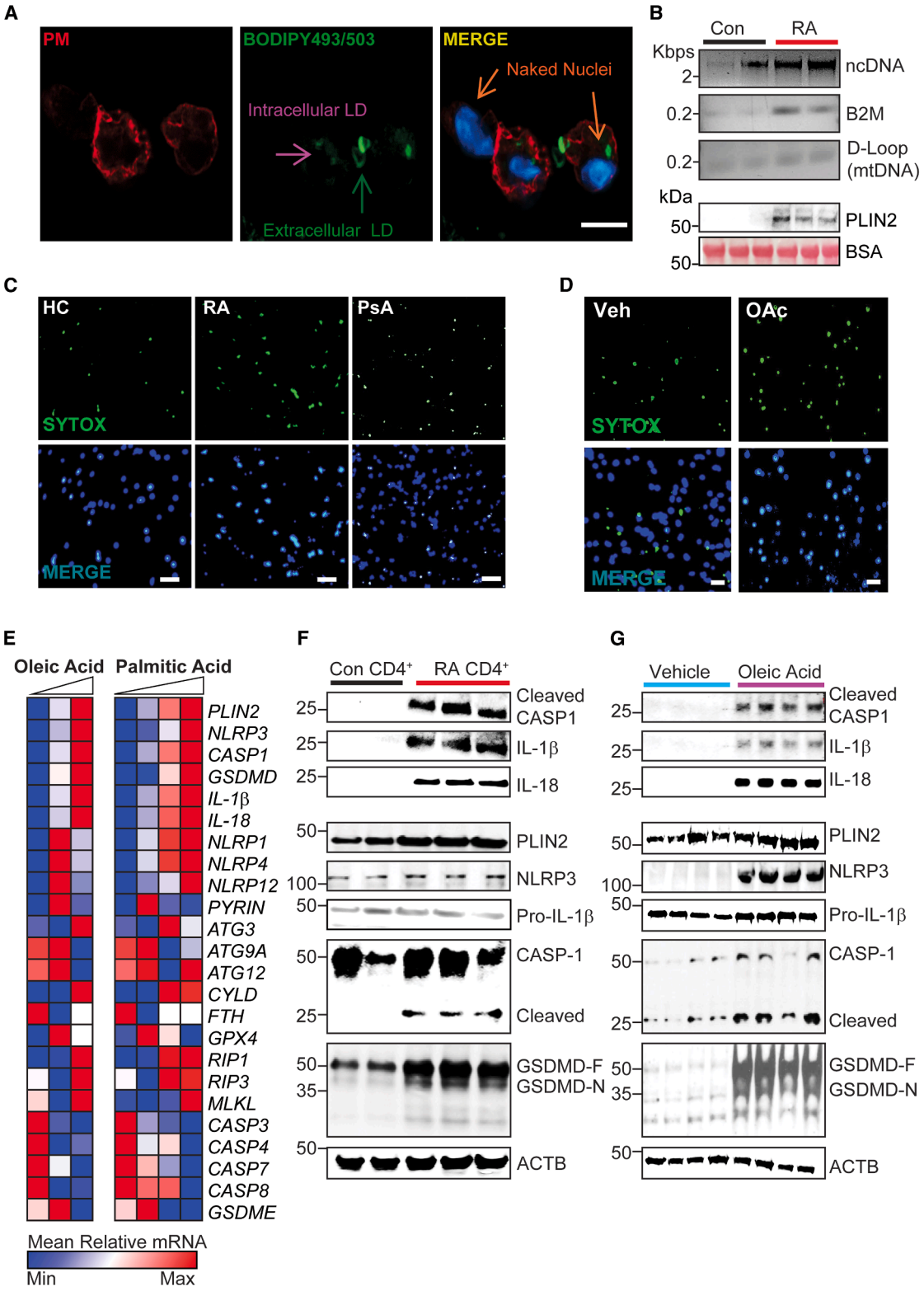

Figure 5. Fatty acids induce pyroptotic T cell death

(A) BODIPY493/503 staining of CD4⁺ T cells isolated from synovial tissue biopsies. PMs marked with WGA (red) and nuclei with DAPI. Scale bar, 5 μm.

(B) Control and RA CD4⁺ T cells were activated for 72 h and treated with OAc for 1 h. Immunoblot analysis of supernatants for nuclear DNA (ncDNA), β2-microglobulin (B2M), D-loop amplified DNA, and free PLIN2. Representative blots from three experiments.

(C) Representative live-cell images showing SYTOX-green uptake in CD4⁺ T cells from healthy controls, RA, and PsA (n = 6/group). Scale bar, 20 μm.

(legend continued on next page)

Please cite this article in press as: Kumar et al., Lipid droplet-induced T cell death sustains autoimmune tissue inflammation, Cell Metabolism (2026), https://doi.org/10.1016/j.cmet.2026.01.014

overexpression (PLIN2-OE) resulted in the following: (1) higher density of inflammatory cell infiltrates (Figure 7G); (2) accumulation of dysmorphic nuclei indicating cell death (Figure 7H); (3) higher frequencies of CD3$^+$ T cells, specifically, IFN-γ-producing T cells, BODIPY$^+$(LD-containing) T cells, and T-bet$^+$ CD4$^+$ T cells (Figure 7I); (4) higher expression of inflammatory cytokine genes (*IL-1β*, *IFN-γ*, *TNF*, *IL-6*, and *IL-17A*); (5) higher expression of T cell lineage-determining transcription factors (*TBx21*; *RORC*) (Figure S9C); and (6) diffuse deposition of BODIPY$^+$ LD in the extracellular space (Figure 7J).

Conversely, we knocked down *PLIN2* selectively in CD4$^+$ T cells (Figures S9D–S9H). Mice receiving *PLIN2*-silenced CD4$^+$ T cells displayed markedly reduced synovial tissue inflammation, with significantly fewer dead cells, BODIPY$^+$CD3$^+$ T cells, and CD3$^+$-IFN-γ$^+$ and CD3$^+$T-bet$^+$ T cells. Transfer of *PLIN2*-deficient CD4$^+$ T cells quickly lowered the LD deposits in the tissue (Figures 7K–7N).

In vitro experiments validated that PLIN2-OE had a profound impact on the lineage commitment of CD4$^+$ T cells and was sufficient to turn them into pro-inflammatory effector cells. PLIN2^{hi}-expressing CD4$^+$ T cells responded to lipid exposure with rapid differentiation into T-bet$^+$ and RORγt$^+$ T cells that were committed to the production of inflammatory cytokines, including IFN-γ, IL-17, and IL-21 (Figures S10A–S10F).

These results identify LDs in T cells as pro-inflammatory organelles and demonstrate their therapeutic targetability in autoimmune tissue inflammation.

DISCUSSION

Traditional paradigms have focused on autoantigens as key factors in autoimmune disease, linking pathogenic T cell function to antigen specificity. However, current data challenge this notion, showing that CD4$^+$ T cells can instigate tissue inflammation through pyroptosis, releasing danger-associated molecular patterns (DAMPs). Underlying mechanisms connect the metabolic constraints in nutrient-stressed tissues to T cell stress responses and to pro-inflammatory, lytic cell death. We reveal a novel pathway where CD4$^+$ T cells in the lipid-rich rheumatoid joint form LDs that sequester the pore-forming molecule GSDMD and its zDHHC5 S-acylase. Under lipid stress, GSDMD$^+$ zDHHC5$^+$ LDs move to the PM and create membrane pores, releasing nuclear and cytosolic content, including intact LDs that promote continued lipid accumulation at inflammatory sites. Our data show that RA CD4$^+$ T cells are primed to support this disease mechanism due to their metabolic conditioning that includes severe mitochondrial impairment, suppressed lipolysis, and enhanced LD formation. In humanized mice, inhibiting LD formation or blocking global S-acylation in RA CD4$^+$ T cells is sufficient to reduce synovitis (Figure 7). Conversely, enforcing LD formation in healthy CD4$^+$ T cells transforms these T cells into tissue-damaging effector cells and effectively breaks tissue tolerance, highlighting this metabolic pathway as a crucial checkpoint in autoimmune disease.

Classically, LDs are recognized as cytosolic fat storage organelles that supply lipids based on bioenergetic needs.[17,19,44–46] Data presented here redefine the role of LDs in CD4$^+$ T cells, revealing that LDs act as pro-death organelles that move to the PM and cause membrane leakage and lytic cell death. This transformation from protective to damage-inducing organelles requires a change in the LD proteome. Specifically, the sequestration of GSDMD and zDHHC5 to GSDMD$^+$zDHHC5$^+$ LDs links lipid metabolism abnormalities and pyroptotic T cell death to synovitis.

The shift in the LD proteome occurs in RA CD4$^+$ T cells, which have reconfigured their bioenergetic networks and have entered a state of pseudo-starvation. Due to mitochondrial DNA repair defects,[3] they exhibit low mitochondrial fitness with diminished ATP and NAD production.[15,47] These T cells adapt by downregulating glycolysis and redirecting glucose into the pentose-phosphate pathway,[15,48] resulting in elevated NADPH and intensified lipogenesis.[47] A lack of mitochondrial β-oxidation further drives lipid synthesis[12] and boosts cytosolic acetyl-CoA and citrate levels.[15] Low ATP and NAD$^+$ suggest that RA CD4$^+$ T cells are in starvation mode, barely able to meet bioenergetic and biosynthetic needs. Prior studies indicate that this pseudo-starvation mode[49] affects most RA T cells,[49] broadly impacting the immune system beyond rare antigen-specific T cells.[13] The cause of this metabolic transformation in RA CD4$^+$ T cells is unexplained but renders this cell population susceptible to non-canonical functions, such as membrane lysis and DAMP release, which may be particularly relevant in disease chronicity.

Mitochondrial failure and pseudo-starvation trigger cellular stress responses.[10,49,50] Accordingly, RA CD4$^+$ T cells exhibit lysosomal deficiencies[51,52] and are under ER stress.[4,14] ER stress responses involve remodeling lipid metabolism, storing lipids in LDs, and preparing cells for high metabolic demands.[46,53,54] T cell receptor (TCR) stimulation of RA CD4$^+$ T cells induces ER stress and formation of large LDs, as these cells anticipate clonal expansion with high bioenergetic and biosynthetic demands. CD4$^+$ T cells from inflamed joints displayed the highest susceptibility to LD-dependent cell lysis, suggesting a state of metabolic burnout. Both joint-derived and circulating-RA CD4$^+$ T cells upregulated *PLIN2* and accumulated LD, placing the metabolic adaptations prior to these cells entering disease lesions. Inflammasome activation upstream of GSDMD activation is frequent in lymph node T cells of patients with RA,[3,11] suggesting that lymphoid tissues prime RA CD4$^+$ T cells for low metabolic resilience.

Chronic inflammation sites, like the tumor microenvironment, represent nutrient-stressed niches.[55] RA CD4$^+$ T cells face challenging metabolic conditions when infiltrating glucose-deplete synovial tissue.[9] Educated under conditions of poor

(D) Representative live-cell images showing SYTOX-green uptake in CD4$^+$ T cells treated with OAc (10 μg/mL, 6 h) (n = 6/group). Scale bar, 20 μm.
(E) Control CD4$^+$ T cells were treated with OAc (0, 10, and 25 μg/mL) or PA (0, 1, 2, and 5 μM) for 6 h. Heatmap of mean relative mRNAs from three experiments.
(F) Control and RA CD4$^+$ T cells were stimulated for 72 h. Supernatants were analyzed for CASP1, IL-1β, and IL-18. Cell lysates were analyzed for PLIN2, NLRP3, PLIN3, CASP1, GSDMD, and β-actin. Representative immunoblots from three experiments.
(G) Control CD4$^+$ T cells were treated with vehicle or OAc (10 μg/mL, 6 h). Supernatants were analyzed for CASP1, IL-1β, and IL-18. Cell lysates were analyzed for PLIN2, NLRP3, PLIN3, CASP1, GSDMD, and β-actin. Representative immunoblots from four experiments.

Please cite this article in press as: Kumar et al., Lipid droplet-induced T cell death sustains autoimmune tissue inflammation, Cell Metabolism (2026), https://doi.org/10.1016/j.cmet.2026.01.014

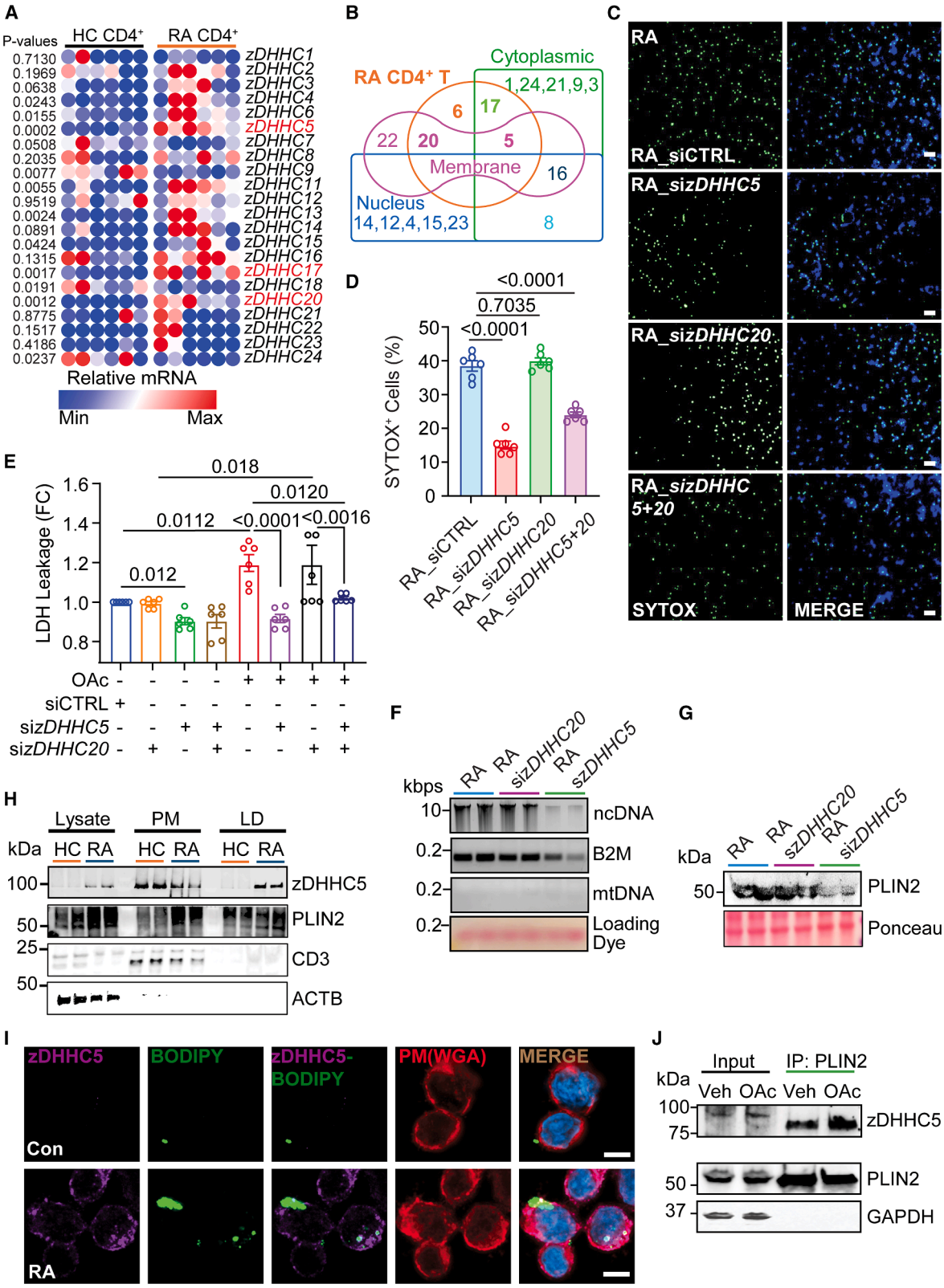

Figure 6. LDs from RA CD4⁺ T cells transport the acyltransferase zDHHC5

CD4⁺CD45RO⁻ T cells from controls and RA patients were stimulated for 72 h.

(A) Relative mRNAs of *hzDHHCs* in control and RA CD4⁺ T cells (n = 6/group).

(legend continued on next page)

Please cite this article in press as: Kumar et al., Lipid droplet-induced T cell death sustains autoimmune tissue inflammation, Cell Metabolism (2026), https://doi.org/10.1016/j.cmet.2026.01.014

mitochondrial performance, these T cells become less reliant on glucose, gaining a survival advantage in the synovial space. Targeted metabolomics have revealed high levels of glutamine in RA synovium.[9] However, glutaminolysis requires a functional TCA cycle, which is compromised in RA CD4$^+$ T cells, forcing them to depend on FFAs for energy. Given that high FFA concentrations are typical in atherosclerotic lesions, T cells may experience similar nutrient stress within atherosclerotic plaques, which may explain the increased cardiovascular risk in RA.[56]

While the role of metabolites in DNA and histone acetylation and methylation links nutrient supply with epigenetic regulation, data presented here deepen understanding of how metabolites regulate posttranslational protein modifications.[38] Notably, RA CD4$^+$ T cells exhibit defects in protein N-myristylation.[51] The current study identifies protein palmitoylation as a critical checkpoint for T cell differentiation and membrane integrity. The cleavage of the pore-forming molecule GSDMD requires S-acylation, with FASN providing the substrate needed in this modification.[38] An S-acylase positioned upstream of GSDMD activation indicates that membrane pore formation occurs preferentially in lipid-rich environments, like the rheumatoid joint, underscoring how tissue nutrient availability dictates T cell functionality.

Current data emphasize that LD formation is host-damaging, precisely, by inducing tissue inflammation. Genetic polymorphisms linked to RA susceptibility reside in genes vital for CD4$^+$ T cell function. Traditional effector functions include cytokine production, help for autoantibody-producing B cells, and T cell cytotoxicity. Current insights expand pathogenic T cell functions to include lytic cell death. While T cells typically die via anti-inflammatory apoptosis, lipid-induced pore formation leads to cell lysis and DAMP release. T cell supernatants contained nuclear and cytosolic contents, including nuclear DNA and PLIN2. OAc and PA upregulated a gene signature linked to inflammasome components, inflammatory CASPs, IL-1, and IL-18, all characteristics of pyroptosis. These findings support a model where tissue-resident T cells, under lipid stress and lacking metabolic plasticity, undergo pyroptosis instead of apoptosis. This shift has significant implications; while apoptotic T cells are quietly cleared, pyroptotic T cells release immunogenic DAMPs, including mitochondrial and nuclear DNA, perpetuating synovial inflammation even without antigenic stimulation. Therefore, T cell pyroptosis may be a key mechanism underlying the self-sustaining nature of rheumatoid synovitis.

One surprising finding in this study is LD-based sequestration of GSDMD. Through proteomic analysis, immunoblotting, and immunofluorescence, we showed that GSDMD is enriched in the LD fraction and co-localizes with PLIN2 in the T cell uropod. Upon lipid stress, GSDMD$^+$LDs translocated to the PM, promoting pore formation. RA CD4$^+$ T cells also co-packaged zDHHC5 into the LD, with functional assays confirming the cytoprotective effects of inhibiting S-acylation *in vitro* and *in vivo*. Normally, GSDMD and the lipidating enzyme are kept in separate compartments (cytosol and PM), preventing spontaneous GSDMD activation. However, lipid-induced cellular stress disrupts this protective mechanism, leading to membrane translocation of GSDMD$^+$zDHHC5$^+$LDs and LD release into the extracellular space. Conceivably, GSDMD$^+$zDHHC5$^+$LDs could provide an outlet for excess lipids being expelled from the cell. In the rheumatoid joint, possibly due to high FFA concentrations, safe release of LDs is replaced by membrane disintegration, contaminating the tissue with ever-growing FFA deposits and sustaining a feedforward loop of tissue inflammation.

Paradoxically, inflammation-inducing LDs were enriched for OAc, a monounsaturated fatty acid often classified as a "healthy fat."[57,58] The effect of OAc and PA on inducing lytic T cell death was indistinguishable, suggesting that all FFAs are potentially pathogenic, if the absorbing T cell fails to catabolize lipids and to utilize them for enhanced functionality. Patients with RA are at substantial risk for cardiovascular complications, and intriguingly, OAc is also a significant component of the FFA profile in atherosclerotic plaque,[59,60] pointing toward shared lipid-induced pathomechanisms in RA and atherosclerosis.

In conclusion, our data define a novel, metabolically controlled mechanism of inflammatory cell death in RA CD4$^+$ T cells. Metabolic pre-conditioning leads to the accumulation of LDs that integrate into the PM to facilitate GSDMD-dependent pyroptosis. This process is ultimately regulated by zDHHC5, which enables membrane-near GSDMD activation and acts as a bridge between abnormal lipid handling and pro-inflammatory cell death.

Current RA therapies mainly focus on cytokine inhibition and general immunosuppression, but our findings suggest a new therapeutic approach, restoring metabolic resilience or blocking lipid-triggered pyroptosis in tissue-resident T cells. We demonstrate that genetic and pharmacological inhibition of PLIN2 or zDHHC5 significantly reduces inflammation *in vivo*. Notably, treatment with 2-BP or CMA, both broad-spectrum S-acylation inhibitors, preserved PM integrity, reduced DAMP release and suppressed immune cell infiltration into synovial tissue without depleting T cells or impairing antigen recognition, indicating a selective anti-inflammatory mechanism. The importance of LDs and zDHHC5 in this pathway may also lead to biomarker development; high expression of PLIN2, GSDMD, CASP1, or zDHHC5 in circulating T cells could identify patients at risk for severe

(B) Predicted subcellular localization of hzDHHC enzymes summarized in a Venn diagram.[39,41]
(C–G) RA CD4$^+$ T cells were transfected with *con*_siRNA, *hzDHHC5*_siRNA, *hzDHHC20*_siRNA, or both and treated with vehicle or OAc for 6 h.
(C) Live-cell images for SYTOX-green uptake (n = 6/group). Scale bar, 100 μm.
(D) Quantification of SYTOX$^+$ T cells (n = 6 experiments).
(E) Quantification of LDH leakage after treatment with vehicle or OAc for 6 h (n = 6/group).
(F) Supernatants were analyzed on agarose gels and native-PCR (B2M for ncDNA and D-loop for mitochondrial DNA) (n = 2/group).
(G) Representative immunoblotting of supernatants for released PLIN2 (n = 2/group).
(H) PM and LD fractions were isolated and immunoblotted for zDHHC5, PLIN2, CD3, and β-actin. Two samples/group from three experiments.
(I) Immunofluorescence staining of hzDHHC5 and BODIPY in control and RA CD4$^+$ T cells. Scale bar, 10 μm.
(J) PLIN2 was immunoprecipitated from vehicle- and OAc-treated RA CD4$^+$ T cells. Precipitates were immunoblotted for zDHHC5. One of three experiments shown.
All data are mean ± SEM with individual values shown. One-way ANOVA and Dunnett's multiple comparisons test (D and E).

Please cite this article in press as: Kumar et al., Lipid droplet-induced T cell death sustains autoimmune tissue inflammation, Cell Metabolism (2026), https://doi.org/10.1016/j.cmet.2026.01.014

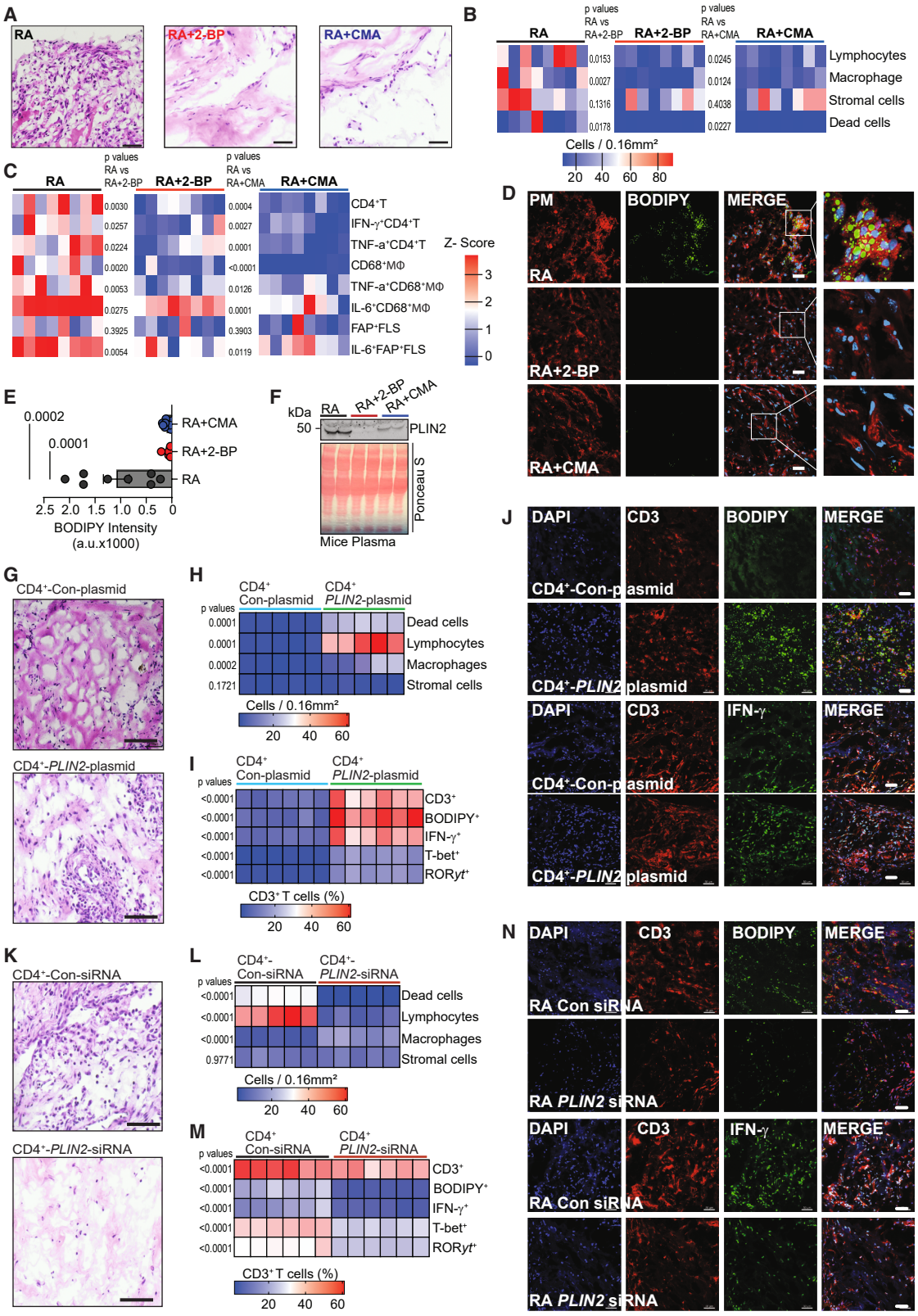

Figure 7. Inhibition of zDHHC5-mediated palmitoylation or blocking LD formation in CD4⁺ T cells abrogates synovial tissue inflammation

(A–F) NSG mice engrafted with human synovium were immunoreconstituted with PBMCs from RA patients. Chimeras were treated intraperitoneally with vehicle, 2-BP (20 mg/kg), or CMA (20 mg/kg) for 1 week. Synovial grafts were collected for histology and flow cytometry. Each group included eight tissues.

(legend continued on next page)

Please cite this article in press as: Kumar et al., Lipid droplet-induced T cell death sustains autoimmune tissue inflammation, Cell Metabolism (2026), https://doi.org/10.1016/j.cmet.2026.01.014

disease or poor response to conventional therapies. Targeting lipid metabolism or specific S-acylation inhibitors may effectively protect vulnerable immune cells from lytic death and provide treatment for challenging RA cases.

Limitations of the study

While our model establishes a causal link between altered lipid metabolism, lytic T cell death, and sustained tissue inflammation, several questions remain. First, the upstream triggers for the upregulation of PLIN2, GSDMD, and zDHHC5 in RA CD4$^+$ T cells, required for the priming of these cells, need further investigation. Although fatty acid exposure may induce these genes, the mechanisms by which cells recognize extracellular lipids and adapt their lipid metabolism and organelle function, and do so over decades, all remain undefined.

Second, the broader relevance of this pathway to other T cell subsets and autoimmune contexts is unknown. Similar mechanisms might operate in CD8$^+$ T cells, regulatory T cells, or tissue-resident memory cells within lipid-rich tissues (e.g., adipose tissue, liver, and CNS). Exploring whether LD-GSDMD interactions influence T cell fate in obesity-related inflammation or neuroinflammation will be an important next step.

Finally, while our *in vivo* model recapitulates essential features of human synovitis, future studies using spatial transcriptomics or single-cell proteomics could yield deeper insights into the tissue microenvironment and identify additional metabolic checkpoints that regulate tissue inflammation.

RESOURCE AVAILABILITY

Lead contact

Further information and requests for resources and reagents should be directed to the lead contact, Cornelia M. Weyand (cweyand@stanford.edu).

Materials availability

Plasmids are available upon request.

Data and code availability

Source data and original blots are included in Data S1. This manuscript did not generate new code.

ACKNOWLEDGMENTS

This work was supported by the United States National Institutes of Health (R01AG045779, R01AI108891, R01AI108906, R01HL117913, R01HL142068, U01AI179609, R01AR042527, R01AI184360, and R01AI129191), the Encrantz Family and Southwell Family Discovery funds, and the Mark and Mary Davis Initiative in Rheumatoid Arthritis.

AUTHOR CONTRIBUTIONS

Conceptualization, C.M.W., J.J.G., and J.K.; methodology, J.K., Y.T., J.M., G.J.B., and I.N.G.; investigation, J.K., Y.T., J.M., B.W., L.W., and S.R.; writing – original draft, C.M.W., J.K., and I.N.G.; writing – review & editing, C.M.W., J.K., I.N.G., G.J.B., and J.J.G.; funding acquisition, C.M.W. and J.J.G.; resources, Y.T., R.T.T., S.R., G.J.B., and J.M.; supervision, C.M.W. and J.J.G.

DECLARATION OF INTERESTS

C.M.W. has received consulting fees from AbbVie, Bristol Myers Squibb, Novartis, Ono Pharmaceutical, Boehringer Ingelheim, and Sparrow Pharmaceuticals. J.J.G. has received consulting fees and stock options from Retro Biosciences.

STAR★METHODS

Detailed methods are provided in the online version of this paper and include the following:

- KEY RESOURCES TABLE
- EXPERIMENTAL MODEL AND STUDY PARTICIPANT DETAILS
  - Patients
  - Synovial tissue samples
  - Human-chimeric NSG mice
- METHOD DETAILS
  - Cells and tissues
  - Fatty acid quantification
  - LD fractionation and Lipidomics

(A) H&E images of synovial explants from vehicle-, 2-BP-, and CMA-treated chimeric mice. Scale bar, 50 μm.
(B) Histomorphometric analysis of explanted synovial tissues. Cell populations were quantified by digital analysis of H&E-stained images. Each dot represents an individual high-power field.
(C) Synovial explants were digested and analyzed by flow cytometry. All numbers are normalized to tissue weight (cells/gram). Frequencies of CD4$^+$ T cells, IFN-γ$^+$CD4$^+$ T cells, TNF$^+$CD4$^+$ T cells, CD68$^+$ macrophages, TNF$^+$CD68$^+$ macrophages, IL-6$^+$CD68$^+$ macrophages, FAP$^+$ synovial fibroblasts, and IL-6$^+$FAP$^+$ fibroblasts are presented as heatmap. Each lane represents one tissue.
(D and E) Synovial tissue sections were stained with BODIPY493/503. Membranes were marked with WGA and nuclei with DAPI. Scale bar, 20 μm. BODIPY493/503 intensity was quantified.
(F) Immunoblot of human PLIN2 in mouse plasma. Loading control, Ponceau S. Data from two mice are shown.
(G–N) NSG mice engrafted with human synovial tissue were randomly assigned to four study arms.
(G–J) Control CD4$^+$CD45RO$^-$ T cells were transfected with either a control plasmid (arm-1) or PLIN2 plasmid (arm-2).
(K–N) RA CD4$^+$CD45RO$^-$ T cells were transfected with either control small interfering RNA (siRNA) (arm-3) or *PLIN2* siRNA (arm-4). Transfected T cells were adoptively transferred into the tissue-engrafted mice. Each arm included six tissues. Explanted synovial grafts were analyzed by flow cytometry, RT-qPCR, and immunohistochemistry.
(G) H&E images from synovial explants. Scale bars, 50 μm.
(H and I) Frequencies of lymphocytes, macrophages, stromal cells, and dead cells were measured by histomorphometry. Frequencies of tissue-infiltrating CD3$^+$ T cells, BODIPY$^+$CD3$^+$ T cells, IFN-γ$^+$CD3$^+$ T cells, T-bet$^+$CD3$^+$ T cells, and RORγτ$^+$CD3$^+$ T cells were determined by flow cytometry. Data presented as heatmap.
(J) Immunofluorescence staining of tissue sections for BODIPY493/503, IFN-γ, and CD3$^+$ T cells.
(K) H&E images from synovial explants. Scale bars, 50 μm.
(L and M) Frequencies of lymphocytes, macrophages, stromal cells, and dead cells quantified by histomorphometric analysis. Frequencies of tissue-infiltrating CD3$^+$ lymphocytes, BODIPY$^+$CD3$^+$ T cells, IFN-γ$^+$CD3$^+$ T cells, T-bet$^+$CD3$^+$ T cells, and RORγτ$^+$CD3$^+$ T cells measured by flow cytometry. Data presented as heatmap, with each lane representing one tissue.
(N) Synovial tissue sections stained for BODIPY493/503, IFN-γ, and CD3$^+$ T cells.
All data are mean ± SEM with individual values shown. One-way ANOVA and Dunnett's multiple comparisons test (B, C, and F). Two-tailed, unpaired Mann-Whitney-Wilcoxon rank test (H, I, L, and M).

- Plasma Membrane fractionation
- Acetyl-CoA quantification
- Intracellular ATP Quantification
- T Cell Transfections
- Real Time PCR
- Flow cytometry
- Immunofluorescence and confocal microscopy
- Transmission electron microscopy
- Live cell imaging
- Subcellular organelle analysis
- Cell Size Analysis
- Histomorphometry of Synovial tissue
- Cell membrane leakiness, SYTOX Green Uptake, and lytic cell death
- Lactate Dehydrogenase Quantification
- IL-1β Release Assay
- Extracellular DNA Quantification
- Quantification of Extracellular LD
- Cell-Free Nuclear DNA and Lipid Droplets in Mouse Plasma
- Immunoblotting
- Immunoprecipitation
- Mass spectrometry analysis

- QUANTIFICATION AND STATISTICAL ANALYSIS

SUPPLEMENTAL INFORMATION

Supplemental information can be found online at https://doi.org/10.1016/j.cmet.2026.01.014.

Received: July 15, 2025
Revised: November 13, 2025
Accepted: January 26, 2026

REFERENCES

1. Conrad, N., Misra, S., Verbakel, J.Y., Verbeke, G., Molenberghs, G., Taylor, P.N., Mason, J., Sattar, N., McMurray, J.J.V., McInnes, I.B., et al. (2023). Incidence, prevalence, and co-occurrence of autoimmune disorders over time and by age, sex, and socioeconomic status: a population-based cohort study of 22 million individuals in the UK. Lancet *401*, 1878–1890. https://doi.org/10.1016/S0140-6736(23)00457-9.

2. Lee, Y.S., and Olefsky, J. (2021). Chronic tissue inflammation and metabolic disease. Genes Dev. *35*, 307–328. https://doi.org/10.1101/gad.346312.120.

3. Li, Y., Shen, Y., Jin, K., Wen, Z., Cao, W., Wu, B., Wen, R., Tian, L., Berry, G.J., Goronzy, J.J., et al. (2019). The DNA repair nuclease MRE11A functions as a mitochondrial protector and prevents T cell pyroptosis and tissue inflammation. Cell Metab. *30*, 477–492.e6. https://doi.org/10.1016/j.cmet.2019.06.016.

4. Weyand, C.M., and Goronzy, J.J. (2021). The immunology of rheumatoid arthritis. Nat. Immunol. *22*, 10–18. https://doi.org/10.1038/s41590-020-00816-x.

5. Qiu, J., Wu, B., Goodman, S.B., Berry, G.J., Goronzy, J.J., and Weyand, C.M. (2021). Metabolic control of autoimmunity and tissue inflammation in rheumatoid arthritis. Front. Immunol. *12*, 652771. https://doi.org/10.3389/fimmu.2021.652771.

6. Weyand, C.M., and Goronzy, J.J. (2025). Immune aging in rheumatoid arthritis. Arthritis Rheumatol. *77*, 792–804. https://doi.org/10.1002/art.43105.

7. Chemin, K., Gerstner, C., and Malmström, V. (2019). Effector functions of CD4+ T cells at the site of local autoimmune inflammation-lessons from rheumatoid arthritis. Front. Immunol. *10*, 353. https://doi.org/10.3389/fimmu.2019.00353.

8. Macallan, D.C., Wallace, D., Zhang, Y., De Lara, C., Worth, A.T., Ghattas, H., Griffin, G.E., Beverley, P.C.L., and Tough, D.F. (2004). Rapid turnover of effector-memory CD4(+) T cells in healthy humans. J. Exp. Med. *200*, 255–260. https://doi.org/10.1084/jem.20040341.

9. Hu, Z., Zhao, T.V., Huang, T., Ohtsuki, S., Jin, K., Goronzy, I.N., Wu, B., Abdel, M.P., Bettencourt, J.W., Berry, G.J., et al. (2022). The transcription factor RFX5 coordinates antigen-presenting function and resistance to nutrient stress in synovial macrophages. Nat. Metab. *4*, 759–774. https://doi.org/10.1038/s42255-022-00585-x.

10. Weyand, C.M., Wu, B., and Goronzy, J.J. (2020). The metabolic signature of T cells in rheumatoid arthritis. Curr. Opin. Rheumatol. *32*, 159–167. https://doi.org/10.1097/BOR.0000000000000683.

11. Li, Y., Goronzy, J.J., and Weyand, C.M. (2018). DNA damage, metabolism and aging in pro-inflammatory T cells: Rheumatoid arthritis as a model system. Exp. Gerontol. *105*, 118–127. https://doi.org/10.1016/j.exger.2017.10.027.

12. Shen, Y., Wen, Z., Li, Y., Matteson, E.L., Hong, J., Goronzy, J.J., and Weyand, C.M. (2017). Metabolic control of the scaffold protein TKS5 in tissue-invasive, proinflammatory T cells. Nat. Immunol. *18*, 1025–1034. https://doi.org/10.1038/ni.3808.

13. Weyand, C.M., and Goronzy, J.J. (2025). Metabolic checkpoints in rheumatoid arthritis. Semin. Arthritis Rheum. *70S*, 152586. https://doi.org/10.1016/j.semarthrit.2024.152586.

14. Wu, B., Zhao, T.V., Jin, K., Hu, Z., Abdel, M.P., Warrington, K.J., Goronzy, J.J., and Weyand, C.M. (2021). Mitochondrial aspartate regulates TNF biogenesis and autoimmune tissue inflammation. Nat. Immunol. *22*, 1551–1562. https://doi.org/10.1038/s41590-021-01065-2.

15. Wu, B., Qiu, J., Zhao, T.V., Wang, Y., Maeda, T., Goronzy, I.N., Akiyama, M., Ohtsuki, S., Jin, K., Tian, L., et al. (2020). Succinyl-CoA ligase deficiency in pro-inflammatory and tissue-invasive T cells. Cell Metab. *32*, 967–980.e5. https://doi.org/10.1016/j.cmet.2020.10.025.

16. Hunt, E.G., Hurst, K.E., Riesenberg, B.P., Kennedy, A.S., Gandy, E.J., Andrews, A.M., Del Mar Alicea Pauneto, C., Ball, L.E., Wallace, E.D., Gao, P., et al. (2024). Acetyl-CoA carboxylase obstructs $CD8^+$ T cell lipid utilization in the tumor microenvironment. Cell Metab *36*, 969–983.e10. https://doi.org/10.1016/j.cmet.2024.02.009.

17. Olzmann, J.A., and Carvalho, P. (2019). Dynamics and functions of lipid droplets. Nat. Rev. Mol. Cell Biol. *20*, 137–155. https://doi.org/10.1038/s41580-018-0085-z.

18. Jarc, E., and Petan, T. (2019). Lipid droplets and the management of cellular stress. Yale J. Biol. Med. *92*, 435–452.

19. Mathiowetz, A.J., and Olzmann, J.A. (2024). Lipid droplets and cellular lipid flux. Nat. Cell Biol. *26*, 331–345. https://doi.org/10.1038/s41556-024-01364-4.

20. Roberts, M.A., Deol, K.K., Mathiowetz, A.J., Lange, M., Leto, D.E., Stevenson, J., Hashemi, S.H., Morgens, D.W., Easter, E., Heydari, K., et al. (2023). Parallel CRISPR-Cas9 screens identify mechanisms of PLIN2 and lipid droplet regulation. Dev. Cell *58*, 1782–1800.e10. https://doi.org/10.1016/j.devcel.2023.07.001.

21. Bezawork-Geleta, A., Devereux, C.J., Keenan, S.N., Lou, J., Cho, E., Nie, S., De Souza, D.P., Narayana, V.K., Siddall, N.A., Rodrigues, C.H.M., et al. (2025). Proximity proteomics reveals a mechanism of fatty acid transfer at lipid droplet-mitochondria- endoplasmic reticulum contact sites. Nat. Commun. *16*, 2135. https://doi.org/10.1038/s41467-025-57405-5.

22. Krahmer, N., and Mann, M. (2019). Catching lipid droplet contacts by proteomics. Contact (Thousand Oaks) *2*, 2515256419859186. https://doi.org/10.1177/2515256419859186.

23. Liang, J.J., Fraser, I.D.C., and Bryant, C.E. (2021). Lipid regulation of NLRP3 inflammasome activity through organelle stress. Trends Immunol. *42*, 807–823. https://doi.org/10.1016/j.it.2021.07.005.

24. Bosch, M., Sánchez-Álvarez, M., Fajardo, A., Kapetanovic, R., Steiner, B., Dutra, F., Moreira, L., López, J.A., Campo, R., Marí, M., et al. (2020). Mammalian lipid droplets are innate immune hubs integrating cell metabolism and host defense. Science *370*, eaay8085. https://doi.org/10.1126/science.aay8085.

25. Bosch, M., Parton, R.G., and Pol, A. (2020). Lipid droplets, bioenergetic fluxes, and metabolic flexibility. Semin. Cell Dev. Biol. *108*, 33–46. https://doi.org/10.1016/j.semcdb.2020.02.010.

26. Bosch, M., Sweet, M.J., Parton, R.G., and Pol, A. (2021). Lipid droplets and the host-pathogen dynamic: FATal attraction? J. Cell Biol. *220*, e202104005. https://doi.org/10.1083/jcb.202104005.

27. Chang, M.H., Levescot, A., Nelson-Maney, N., Blaustein, R.B., Winden, K.D., Morris, A., Wactor, A., Balu, S., Grieshaber-Bouyer, R., Wei, K., et al. (2021). Arthritis flares mediated by tissue-resident memory T cells in the joint. Cell Rep. *37*, 109902. https://doi.org/10.1016/j.celrep.2021.109902.

28. Zhang, F., Jonsson, A.H., Nathan, A., Millard, N., Curtis, M., Xiao, Q., Gutierrez-Arcelus, M., Apruzzese, W., Watts, G.F.M., Weisenfeld, D., et al. (2023). Deconstruction of rheumatoid arthritis synovium defines inflammatory subtypes. Nature *623*, 616–624. https://doi.org/10.1038/s41586-023-06708-y.

29. Mustonen, A.-M., Tollis, S., Käkelä, R., Sihvo, S.P., Palosaari, S., Pohjanen, V.-M., Yli-Hallila, A., Lehenkari, P., and Nieminen, P. (2023). Increased n-6 polyunsaturated fatty acids indicate pro- and anti-inflammatory lipid modifications in synovial membranes with rheumatoid arthritis. Inflammation *46*, 1396–1413. https://doi.org/10.1007/s10753-023-01816-3.

30. Mustonen, A.-M., Käkelä, R., Lehenkari, P., Huhtakangas, J., Turunen, S., Joukainen, A., Kääriäinen, T., Paakkonen, T., Kröger, H., and Nieminen, P. (2019). Distinct fatty acid signatures in infrapatellar fat pad and synovial fluid of patients with osteoarthritis versus rheumatoid arthritis. Arthritis Res. Ther. *21*, 124. https://doi.org/10.1186/s13075-019-1914-y.

31. Kaushik, S., and Cuervo, A.M. (2015). Degradation of lipid droplet-associated proteins by chaperone-mediated autophagy facilitates lipolysis. Nat. Cell Biol. *17*, 759–770. https://doi.org/10.1038/ncb3166.

32. Chiariello, A., Rossetti, L., Valente, S., Pasquinelli, G., Sollazzo, M., Iommarini, L., Porcelli, A.M., Tognocchi, M., Conte, G., Santoro, A., et al. (2024). Downregulation of PLIN2 in human dermal fibroblasts impairs mitochondrial function in an age-dependent fashion and induces cell senescence via GDF15. Aging Cell *23*, e14111. https://doi.org/10.1111/acel.14111.

33. Zhu, C., Xu, S., Jiang, R., Yu, Y., Bian, J., and Zou, Z. (2024). The gasdermin family: emerging therapeutic targets in diseases. Signal Transduct. Target. Ther. *9*, 87. https://doi.org/10.1038/s41392-024-01801-8.

34. Lieberman, J., Wu, H., and Kagan, J.C. (2019). Gasdermin D activity in inflammation and host defense. Sci. Immunol. *4*, eaav1447. https://doi.org/10.1126/sciimmunol.aav1447.

35. Kruse, B., Buzzai, A.C., Shridhar, N., Braun, A.D., Gellert, S., Knauth, K., Pozniak, J., Peters, J., Dittmann, P., Mengoni, M., et al. (2023). $CD4^+$ T cell-induced inflammatory cell death controls immune-evasive tumours. Nature *618*, 1033–1040. https://doi.org/10.1038/s41586-023-06199-x.

36. Sundaram, B., Tweedell, R.E., Prasanth Kumar, S., and Kanneganti, T.D. (2024). The NLR family of innate immune and cell death sensors. Immunity *57*, 674–699. https://doi.org/10.1016/j.immuni.2024.03.012.

37. Zhang, N., Zhang, J., Yang, Y., Shan, H., Hou, S., Fang, H., Ma, M., Chen, Z., Tan, L., and Xu, D. (2024). A palmitoylation–depalmitoylation relay spatiotemporally controls GSDMD activation in pyroptosis. Nat. Cell Biol. *26*, 757–769. https://doi.org/10.1038/s41556-024-01397-9.

38. Balasubramanian, A., Hsu, A.Y., Ghimire, L., Tahir, M., Devant, P., Fontana, P., Du, G., Liu, X., Fabin, D., Kambara, H., et al. (2024). The palmitoylation of gasdermin D directs its membrane translocation and pore formation during pyroptosis. Sci. Immunol. *9*, eadn1452. https://doi.org/10.1126/sciimmunol.adn1452.

39. Ohno, Y., Kihara, A., Sano, T., and Igarashi, Y. (2006). Intracellular localization and tissue-specific distribution of human and yeast DHHC cysteine-rich domain-containing proteins. Biochim. Biophys. Acta *1761*, 474–483. https://doi.org/10.1016/j.bbalip.2006.03.010.

40. Liu, H., Wen, S., Xu, C., Kang, X., and Kong, E. (2025). Mechanisms and functional implications of ZDHHC5 in cellular physiology and disease. J. Lipid Res. *66*, 100793. https://doi.org/10.1016/j.jlr.2025.100793.

41. Malgapo, M.I.P., and Linder, M.E. (2021). Substrate recruitment by zDHHC protein acyltransferases. Open Biol. *11*, 210026. https://doi.org/10.1098/rsob.210026.

42. Lan, T., Delalande, C., and Dickinson, B.C. (2021). Inhibitors of DHHC family proteins. Curr. Opin. Chem. Biol. *65*, 118–125. https://doi.org/10.1016/j.cbpa.2021.07.002.

43. Liu, D., Cruz-Cosme, R., Wu, Y., Leibowitz, J., and Tang, Q. (2024). 2-Bromopalmitate depletes lipid droplets to inhibit viral replication. J. Virol. *98*, e0017124. https://doi.org/10.1128/jvi.00171-24.

44. Zadoorian, A., Du, X., and Yang, H. (2023). Lipid droplet biogenesis and functions in health and disease. Nat. Rev. Endocrinol. *19*, 443–459. https://doi.org/10.1038/s41574-023-00845-0.

45. Cohen, S. (2018). Lipid droplets as organelles. Int. Rev. Cell Mol. Biol. *337*, 83–110. https://doi.org/10.1016/bs.ircmb.2017.12.007.

46. Zhang, S., Lv, K., Liu, Z., Zhao, R., and Li, F. (2024). Fatty acid metabolism of immune cells: a new target of tumour immunotherapy. Cell Death Discov. *10*, 39. https://doi.org/10.1038/s41420-024-01807-9.

47. Yang, Z., Shen, Y., Oishi, H., Matteson, E.L., Tian, L., Goronzy, J.J., and Weyand, C.M. (2016). Restoring oxidant signaling suppresses proarthritogenic T cell effector functions in rheumatoid arthritis. Sci. Transl. Med. *8*, 331ra38. https://doi.org/10.1126/scitranslmed.aad7151.

48. Yang, Z., Fujii, H., Mohan, S.V., Goronzy, J.J., and Weyand, C.M. (2013). Phosphofructokinase deficiency impairs ATP generation, autophagy, and redox balance in rheumatoid arthritis T cells. J. Exp. Med. *210*, 2119–2134. https://doi.org/10.1084/jem.20130252.

49. García-Jiménez, C., and Goding, C.R. (2019). Starvation and pseudo-starvation as drivers of cancer metastasis through translation reprogramming. Cell Metab. *29*, 254–267. https://doi.org/10.1016/j.cmet.2018.11.018.

50. Jin, J., Zhang, H., Weyand, C.M., and Goronzy, J.J. (2021). Lysosomes in T cell immunity and aging. Front. Aging *2*, 809539. https://doi.org/10.3389/fragi.2021.809539.

51. Wen, Z., Jin, K., Shen, Y., Yang, Z., Li, Y., Wu, B., Tian, L., Shoor, S., Roche, N.E., Goronzy, J.J., et al. (2019). N-myristoyltransferase deficiency impairs activation of kinase AMPK and promotes synovial tissue inflammation. Nat. Immunol. *20*, 313–325. https://doi.org/10.1038/s41590-018-0296-7.

52. Zhang, W., Xu, L., Zhu, L., Liu, Y., Yang, S., and Zhao, M. (2021). Lipid droplets, the central hub integrating cell metabolism and the immune system. Front. Physiol. *12*, 746749. https://doi.org/10.3389/fphys.2021.746749.

53. Lim, S.A., Su, W., Chapman, N.M., and Chi, H. (2022). Lipid metabolism in T cell signaling and function. Nat. Chem. Biol. *18*, 470–481. https://doi.org/10.1038/s41589-022-01017-3.

54. Hunt, E.G., Andrews, A.M., Larsen, S.R., and Thaxton, J.E. (2022). The ER-mitochondria interface as a dynamic hub for T cell efficacy in solid tumors. Front. Cell Dev. Biol. *10*, 867341. https://doi.org/10.3389/fcell.2022.867341.

55. Yang, C., Ko, B., Hensley, C.T., Jiang, L., Wasti, A.T., Kim, J., Sudderth, J., Calvaruso, M.A., Lumata, L., Mitsche, M., et al. (2014). Glutamine oxidation maintains the TCA cycle and cell survival during impaired mitochondrial pyruvate transport. Mol. Cell *56*, 414–424. https://doi.org/10.1016/j.molcel.2014.09.025.

56. Johri, N., Varshney, S., Gandha, S., Maurya, A., Mittal, P., Jangra, S., Garg, R., and Saraf, A. (2023). Association of cardiovascular risks in rheumatoid arthritis patients: Management, treatment and future perspectives. Health Sciences Review *8*, 100108. https://doi.org/10.1016/j.hsr.2023.100108.

57. Kremer, J.M. (2000). n-3 fatty acid supplements in rheumatoid arthritis. Am. J. Clin. Nutr. *71*, 349S–351S. https://doi.org/10.1093/ajcn/71.1.349s.

58. Sun, L., Zhu, J., Mi, S., Li, Y., Wang, T., and Li, Y. (2021). Causal association of monounsaturated fatty acids with rheumatoid arthritis but not osteoarthritis: A two-sample Mendelian randomization study. Nutrition *91–92*, 111363. https://doi.org/10.1016/j.nut.2021.111363.

59. Pettinella, C., Lee, S.H., Cipollone, F., and Blair, I.A. (2007). Targeted quantitative analysis of fatty acids in atherosclerotic plaques by high

sensitivity liquid chromatography/tandem mass spectrometry. J. Chromatogr. B Analyt. Technol. Biomed. Life Sci. *850*, 168–176. https://doi.org/10.1016/j.jchromb.2006.11.023.

60. Thies, F., Garry, J.M.C., Yaqoob, P., Rerkasem, K., Williams, J., Shearman, C.P., Gallagher, P.J., Calder, P.C., and Grimble, R.F. (2003). Association of n-3 polyunsaturated fatty acids with stability of atherosclerotic plaques: a randomised controlled trial. Lancet *361*, 477–485. https://doi.org/10.1016/s0140-6736(03)12468-3.
61. Tan, Y., and Buch, M.H. (2022). 'Difficult to treat' rheumatoid arthritis: current position and considerations for next steps. RMD Open *8*, e002387. https://doi.org/10.1136/rmdopen-2022-002387.
62. Buch, M.H., Eyre, S., and McGonagle, D. (2021). Persistent inflammatory and non-inflammatory mechanisms in refractory rheumatoid arthritis. Nat. Rev. Rheumatol. *17*, 17–33. https://doi.org/10.1038/s41584-020-00541-7.
63. Krenn, V., Morawietz, L., Burmester, G.R., Kinne, R.W., Mueller-Ladner, U., Muller, B., and Haupl, T. (2006). Synovitis score: discrimination between chronic low-grade and high-grade synovitis. Histopathology *49*, 358–364. https://doi.org/10.1111/j.1365-2559.2006.02508.x.
64. Najm, A., le Goff, B., Venet, G., Garraud, T., Amiaud, J., Biha, N., Charrier, C., Touchais, S., Crenn, V., Blanchard, F., et al. (2019). IMSYC immunologic synovitis score: A new score for synovial membrane characterization in inflammatory and non-inflammatory arthritis. Jt. Bone Spine *86*, 77–81. https://doi.org/10.1016/j.jbspin.2018.04.004.
65. Li, Y., Shen, Y., Hohensinner, P., Ju, J., Wen, Z., Goodman, S.B., Zhang, H., Goronzy, J.J., and Weyand, C.M. (2016). Deficient activity of the nuclease MRE11A induces T cell aging and promotes arthritogenic effector functions in patients with rheumatoid arthritis. Immunity *45*, 903–916. https://doi.org/10.1016/j.immuni.2016.09.013.
66. Zhao, T.V., Hu, Z., Ohtsuki, S., Jin, K., Wu, B., Berry, G.J., Frye, R.L., Goronzy, J.J., and Weyand, C.M. (2022). Hyperactivity of the CD155 immune checkpoint suppresses anti-viral immunity in patients with coronary artery disease. Nat CardioVasc Res *1*, 634–648. https://doi.org/10.1038/s44161-022-00096-8.
67. Ye, Z., Shen, Y., Jin, K., Qiu, J., Hu, B., Jadhav, R.R., Sheth, K., Weyand, C.M., and Goronzy, J.J. (2021). Arachidonic acid-regulated calcium signaling in T cells from patients with rheumatoid arthritis promotes synovial inflammation. Nat. Commun. *12*, 907. https://doi.org/10.1038/s41467-021-21242-z.
68. Wang, S., Rong, R., Yang, D.M., Fujimoto, J., Yan, S., Cai, L., Yang, L., Luo, D., Behrens, C., Parra, E.R., et al. (2020). Computational staining of pathology images to study the tumor microenvironment in lung cancer. Cancer Res. *80*, 2056–2066. https://doi.org/10.1158/0008-5472.CAN-19-1629.

Please cite this article in press as: Kumar et al., Lipid droplet-induced T cell death sustains autoimmune tissue inflammation, Cell Metabolism (2026), https://doi.org/10.1016/j.cmet.2026.01.014

CellPress
OPEN ACCESS

STAR★METHODS

KEY RESOURCES TABLE

REAGENT or RESOURCE	SOURCE	IDENTIFIER
Antibodies		
ADFP Antibody (Center), 80uL	Abcepta	#AO1838a; Q99541
Adipophilin / Perilipin-2 Monoclonal Mouse Antibody (ADFP/1365)	Abcepta	# AH13123-20; Q99541
ADRP/Perilipin-2 Monoclonal antibody, 20uL	Protein Tech	# 60340-1-Ig; Q99541
Anti-FLAG M2 Magnetic Beads	Sigma-Aldrich	#M8823-1ML
Anti-Flag-Tag Mouse Monoclonal Antibody 30uL	Booster Bio	# M30971-2-30ul; 17F08
ASC/TMS1 (D2W8U) Rabbit mAb	Cell Signaling Technology	#67824; Q9EPB4
Cytochrome c (D18C7) Rabbit mAb	Cell Signaling Technology	#11940; P99999
Caspase-1 Antibody	Cell Signaling Technology	#2225; P29466
Caspase-1 Cleaved (Asp296) (E2G2I) Rabbit mAb	Cell Signaling Technology	#89332; P29452
Caspase-3 Cleaved (Asp175) (5A1E) Rabbit mAb	Cell Signaling Technology	#9664; P42574
Caspase-7 Cleaved (Asp198) (D6H1) Rabbit mAb	Cell Signaling Technology	#8438; P55210
Caspase-8 Cleaved (Asp374) (18C8) Rabbit mAb	Cell Signaling Technology	#9496; Q14790
CD44 Antibody	Cell Signaling Technology	#3578: P16070
Cleaved Gasdermin D (Asp275) (E7H9G) Rabbit mAb	Cell Signaling Technology	#36425; P57764
Cleaved Gasdermin D (N Terminal) Rabbit mAb	Abclonal	#A24059; 38944952
Cleaved Gasdermin E (N terminal) Rabbit mAb	Abclonal	#A26197; NP_004394.1
FABP1 (D2A3X) XP Rabbit mAb	Cell Signaling Technology	#13368; P07148
GAPDH (D4C6R) Mouse mAb	Cell Signaling Technology	#97166; P04406
Gasdermin D (E9S1X) Rabbit mAb	Cell Signaling Technology	#39754; Q9D8T2
Goat anti-Rabbit IgG (H+L) Highly Cross-Adsorbed Secondary Antibody, Alexa Fluor 555	ThermoFisher	#A-21428
HRP-conjugated β-Actin Rabbit mAb (AC028) 50uL	Abclonal	#AC028
HRP-conjugated Goat anti-Rabbit IgG (H+L) (AS014)	Abclonal	#AS014
HRP-conjugated Goat anti-Mouse IgG (H+L) (AS003)	Abclonal	#AS003
High-Capacity Streptavidin Magnetic Beads (CCT-1497)	Vector Laboratories	#CCT-1497
IL-18 (E8P5O) Rabbit mAb #57058	Cell Signaling Technology	#57058; P70380
IL-1β Rabbit pAb (A16288)	Abclonal	#A16288
Magne HaloTag Beads, 1mL	Promega	#G7281
NLRP3 (D2P5E) Rabbit mAb	Cell Signaling Technology	#13158; Q96P20
PERK (EIF2AK3) Antibody (Center), 80uL	Abcepta	# AP8150c; Q9NZJ5
Perilipin-3 (F8T8T) Rabbit mAb	Cell Signaling Technology	#61336; O60664
SOD1 Antibody (Center), 80uL	Abcepta	#AP8733c; P00441
ZDHHC20 Polyclonal Antibody	ThermoFisher	#PA5-101778; Q5W0Z9
ZDHHC5 (E7T4N) Rabbit mAb	Cell Signaling Technology	#79842; Q9C0B5
Mouse monoclonal anti-CD3	Dako	#M725401-2
Rabbit polyclonal anti-Interferon gamma	Abcam	#ab25101; RRID: AB_448613
Brilliant Violet 421 anti-human IFN-g	BioLegend	#502532; RRID: AB_2561398
PE anti-human IL-17A	BioLegend	# 512306; RRID: AB_961394
Goat anti-rabbit IgG (H+L), Alexa Fluor 488	ThermoFisher	#A-11008; RRID: AB_143165

(*Continued on next page*)

Please cite this article in press as: Kumar et al., Lipid droplet-induced T cell death sustains autoimmune tissue inflammation, Cell Metabolism (2026), https://doi.org/10.1016/j.cmet.2026.01.014

Continued

REAGENT or RESOURCE	SOURCE	IDENTIFIER
Goat anti-mouse IgG (H+L), Alexa Fluor 594	ThermoFisher	#A-11032; RRID: AB_2534091
Bacterial and virus strains		
MAX Efficiency DH5Alpha Competent Cells	ThermoFisher	# 18258012
Biological Samples		
Human synovial tissue	Mayo Clinic	N/A
PBMC from healthy donors	Mayo Clinic	N/A
PBMC from patients with RA	Mayo Clinic	N/A
Plasma from healthy donors	Mayo Clinic	N/A
Plasma from patients with RA	Mayo Clinic	N/A
Chemicals, peptides, and recombinant proteins		
All-in-One Optimized PCR Master mix	Promega	# M7122
BODIPY 493/503	ThermoFisher	# D3922
BODIPY 581/591 C11 (Lipid Peroxidation Sensor)	ThermoFisher	#D3861
Bovine Serum Albumin (BSA), Fraction V, Protease Free	Roche	#3117332001
BSA-Palmitate (5 mM)	Cayman Chemical	#29558
BSA-Oleic Acid	Sigma-Aldrich	#O3008
Bovine Serum Albumin Standard Set	Bio-Rad Laboratories	#5000207
Copper (II) sulfate pentahydrate	Sigma-Aldrich	#469130
Concanavalin A from Canavalia ensiformis (Jack bean)	Sigma-Aldrich	#L6397-1MG
Cyano-myracrylamide (CMA)	MedChemExpress	#HY-155938
2-bromopalmitate (2BP)	MedChemExpress	#HY-111770
2-bromopalmitate (2BP)	Sigma-Aldrich	#21604
eBioscience Cell Stimulation Cocktail (500X)	ThermoFisher	# 00-4970-03
High-Capacity cDNA Reverse Transcription Kit	ThermoFisher	# 4374967
Human Recombinant IL-2,	ThermoFisher	#SIL2
Hydroxylamine solution, 10mL	Sigma-Aldrich	#467804-10ML
Normal Goat Serum Blocking Solution (S-1000-20)	Vector Laboratories	#S-1000-20
Palmitic Acid Alkyne, 1mg	Cayman Chemical	# 13266
Protein A/G PLUS-Agarose	SantaCruz Biotechnology	# sc-2003
TurboFect Transfection Reagent,	ThermoFisher	#R0531
SYTOX Green Nucleic Acid Stain - 5 mM Solution in DMSO	ThermoFisher	# S7020
Wheat Germ Agglutinin (WGA) Conjugates, 1mg	Biotium	#29026-1
Nuclease-Free Water, 25ml	Promega	# P119C-C
anti-CD3/anti-CD28 beads	Life Technologies	#11132D
Lymphoprep	Cosmo Bio	# AXS-1115758
RPMI 1640 Medium	ThermoFisher	#11875135
TGX 4-15% SDS-PAGE	Bio-Rad Laboratories	#456-1083
TGX 10% SDS-PAGE	Bio-Rad Laboratories	# 456-1036
Nitrocellulose membranes	Bio-Rad Laboratories	# 1620117
TBS	Bio-Rad Laboratories	#170-6435
Precision Plus Protein Dual Color Standards	Bio-Rad Laboratories	#161-0374
Tris-Glycine-SDS Running Buffer (10X)	N/A	N/A
Tris-Glycine Transfer Buffer	N/A	N/A
Critical commercial assays		
ATP Determination Kit, 200-1,000 assays	ThermoFisher	A22066
Pierce BCA Protein Assay Kits	ThermoFisher	# 23227
CyQUANT LDH Cytotoxicity Assay, fluorescence	ThermoFisher	# C20302
DNeasy Blood and Tissue Kits for DNA Isolation	Qiagen	# 69506

(*Continued on next page*)

Please cite this article in press as: Kumar et al., Lipid droplet-induced T cell death sustains autoimmune tissue inflammation, Cell Metabolism (2026), https://doi.org/10.1016/j.cmet.2026.01.014

Continued

REAGENT or RESOURCE	SOURCE	IDENTIFIER
EasySep Human T Cell Isolation Kit	STEMCELL	#100-0695
ELISA MAX Deluxe Set Human IL-1β	BioLegend	# 437004
LDH-Cytox Assay Kit	BioLegend	#426401
Lipid Droplet Isolation Kit	Cell Biolabs, Inc.	# MET-5011
MojoSort Human CD4 T Cell Isolation Kit	BioLegend	#480130
NE-PER Nuclear and Cytoplasmic Extraction	ThermoFisher	# 78835
Pierce IP Lysis Buffer	ThermoFisher	#87787
RIPA Lysis and Extraction Buffer	ThermoFisher	#89900
Qubit dsDNA Quantification Assay Kits	ThermoFisher	# Q32851
Ribonuclease A Solution, Molecular Biology Grade, 50 mg	ThermoFisher	J61996.MC
ZymoPure II Plasmid Maxiprep Kit	ZymoResearch	#412818
ZymoPure Plasmid Mini Prep Kit	ZymoResearch	#404064
Amaxa Human T Cell Nucleofector Kits	Lonza	# VPA-1002
4% paraformaldehyde	Santa Cruz Biotechnology	# sc-281692
TMRM Deep Red	Invitrogen	# M7514
Mem-PER Plus Membrane Protein Extraction Kit	ThermoFisher	#89842
Fluoroshield with DAPI	Sigma-Aldrich	#F6057-20ML
Direct-zol RNA MiniPrep	Genesee Scientific	# 11-331
Acetyl CoA Assay Kit	Abcam, USA	#AB87546
Deposited data		
Data used to generate all figures	This paper	Data S1-Source
Experimental models: Cell lines		
Jurkat, Clone E6-1	ATCC	#TIB-152
293T/17 SF [HEK 293T/17 SF]	ATCC	# ACS-4500
Primary Human T cells	N/A	N/A
Experimental models: Organisms/strains		
Human Synovium–NSG Mouse Chimeras (Immune Avatar)	Stanford University	N/A
Oligonucleotides		
qPCR primers	This Paper	See Table S2
control siRNA	SantaCruz Biotechnology	sc-37007
Human ADRP (PLIN2) siRNA	SantaCruz Biotechnology	sc-44841
Human zDHHC5 siRNA	SantaCruz Biotechnology	sc-96568
Human zDHHC20 siRNA	SantaCruz Biotechnology	sc-155498
Recombinant DNA		
PLIN2-Halo-tag	Gift from Dr. McNiven	N/A
Software and algorithms		
GraphPad Prism 10	GraphPad software, inc.	RRID: SCR_002798
ImageJ	National Institutes of Health	RRID: SCR_003070
HD-Staining: Histology-based Digital Staining of Pathology Images	UT Southwestern Medical Center	https://lce.biohpc.swmed.edu/maskrcnn/
ZEISS ZEN lite 3.1	Carl Zeiss	RRID: SCR_018163
FlowJo	BD	RRID: SCR_00852

EXPERIMENTAL MODEL AND STUDY PARTICIPANT DETAILS

Patients

Patients enrolled in the study fulfilled 2010 ACR diagnostic criteria for RA and were positive for rheumatoid factor and/or anti-CCP antibodies. All patients with RA (n=173) recruited had active disease. Individuals with a current or previous diagnosis of cancer,

Please cite this article in press as: Kumar et al., Lipid droplet-induced T cell death sustains autoimmune tissue inflammation, Cell Metabolism (2026), https://doi.org/10.1016/j.cmet.2026.01.014

uncontrolled medical disease or non-rheumatic chronic inflammatory syndrome were excluded from enrollment. Patients with a diagnosis of PsA (n=33; age: 59.0 ± 9.2 years; 41.2% females), Systemic Lupus Erythematosus (SLE) (n=6), and Granulomatosis with Polyangiitis (GPA) (n=6) served as disease controls. Demographic and clinical characteristics of RA and PsA patient populations are summarized in Table S2. Healthy age-matched individuals without a personal history of cancer or autoimmune disease were recruited from the Blood Bank of Mayo Clinic Rochester (n=96). All patients and controls provided informed consent and did not receive compensation. All studies were approved by the Institutional Review Board (IRB) at the Mayo Clinic, Rochester, MN, 55905, USA.

Synovial tissue samples

The Institutional Review Board of the Mayo Clinic, Rochester, MN 55905, USA, approved the study and all patients signed informed consent. Synovial tissue samples were collected from synovectomies or total joint replacement surgeries, mostly from patients with refractory RA. Approximately 15% of patients diagnosed with RA have persistent, treatment-refractory inflammation that fails to respond to multiple disease-modifying therapies. These patients continue to have active joint inflammation over years and decades.[61,62] Classified as having difficult-to-treat RA (D2T-RA), these patients provided an important model system for investigating chronic synovial inflammation. All tissue samples derived from the knee joints of patients with active disease. Active disease was defined as the presence of $\geq$6 swollen or tender joints and levels of at least moderate on the physician's and patient's assessments of disease activity. Patients on prednisone higher than 10 mg/day were excluded. Steroid injections into the knee joint in the last 90 days were considered an exclusion criteria for tissue collection. Tissues were assessed for synovial hyperplasia, vascularization, and density of the cellular infiltrate before they were selected for further experiments. Non-inflammatory control tissues derived from individuals with mechanical joint injuries.

Synovial tissue histopathology and synovitis scoring

All tissue samples underwent histopathological evaluation to confirm the absence or presence of synovitis, and the intensity of synovitis was graded. Serial tissue sections (5 μm) spanning a total of 500 μm^3 of tissue were stained with hematoxylin and eosin (H&E). At least two individuals who had undergone training in the histomorphology assessment of synovial tissue provided a score from 2–5 sections (localized 100 μm apart) to create a single grade for each histopathological feature. We used the criteria set by Krenn and colleagues[63] and Najm et al. with slight modifications[64] to provide uniform synovitis scoring for all tissues enrolled into the study. The composite synovitis score included four major parameters to semi-quantitatively classify the degree of synovial inflammation: 1) synovial lining thickness, 2) density of sub-synovial lymphocytic and plasma cell inflammatory cell infiltrate, 3) activation of stromal elements including multinucleated giant cells, and 4) sub-synovial neovascularization. Finally, scores for each histopathological feature were averaged across the number of sections per sample. In the composite inflammation score, median grades for each component were combined and each patient fell into one of the following categories: category 1, none/normal, average grade <2.0; category 2, mild, average grade 2.0 to 6.0; category 3, moderate/severe, average grade >6.0.

Human-chimeric NSG mice

NSG-mice obtained from Jackson Laboratory and maintained in specific pathogen-free conditions at 20–22 °C and on a 12-hour light/dark cycle. All mice had free access to water and standard rodent diet. The synovial tissues were allocated to experiments based on their arrival order in the laboratory. As previously described,[12,47,65] pieces of human synovial tissue were subcutaneously implanted in 8-12-week-old mice. Seven days later, chimeras were reconstituted with healthy or RA PBMC (15 million/mouse) as per experiment requirements. Littermates (both males and females) were used for each independent experiment and randomly assigned to the different experimental groups.

In a series of experiments to evaluate the effect of oleic acid on tissue inflammation, mice reconstituted with healthy PBMC were treated with either vehicle or oleic acid (10 mg/kg body weight). $CD4^+$ T cells were isolated using MojoSort Human $CD4^+$ T Cell Isolation Kits (BioLegend, #480130), transfected with PLIN2 overexpression plasmids or control plasmids, and then remixed with $CD4^+$ T cell-depleted PBMCs before being adoptively transferred into the mice. In other experiments, RA $CD4^+$ T cells were transfected with siRNA targeting PLIN2 or control siRNA, remixed with $CD4^+$ T cell-depleted PBMCs, and adoptively transferred into the mice. Finally, mice reconstituted with RA PBMCs were treated with either vehicle or 2-BP (2-Bromo-Palmitate, 20 mg/kg body weight) or cyano-myracrylamide (CMA, 20 mg/kg body weight) on alternative days for 8 days. At the end of the experiment, synovial tissues were explanted, OCT-embedded (4583; Sakura Finetek USA) or shock-frozen for further experiments (tissue staining and RNA extraction). To reduce variability introduced by the tissue source and the adoptively transferred immune cells, all mice within one experimental series carried tissue from the same donor patient. All protocols were approved by the Institutional Animal Care and Use Committee of the Mayo Clinic.

METHOD DETAILS

Cells and tissues

PBMCs were isolated by density gradient centrifugation using Lymphoprep (STEMCELL Technologies). Total human $CD4^+$T cells were isolated from peripheral blood mononuclear cells (PBMCs) using the EasySep Human $CD4^+$ T Cell Isolation Kit (STEMCELL Technologies) based on an immunomagnetic negative selection strategy. Briefly, PBMCs were resuspended in EasySep buffer and incubated with the supplied antibody isolation cocktail to label non-$CD4^+$ cells, followed by addition of RapidSpheres magnetic particles. The labeled unwanted cells were retained using an EasySep magnet, while the enriched fraction containing untouched

Please cite this article in press as: Kumar et al., Lipid droplet-induced T cell death sustains autoimmune tissue inflammation, Cell Metabolism (2026), https://doi.org/10.1016/j.cmet.2026.01.014

$CD4^+$ T cells was collected, washed, and immediately used for downstream functional and molecular assays.[14] To activate $CD4^+$ T cells, they were cultured in RPMI 1640 medium supplemented with 10% fetal calf serum and anti-CD3/anti-CD28 beads (ratio 1:3) for a duration of 3 days before being used in experiments. To assess the responsiveness of $CD4^+$ T cells to free fatty acids, they were treated with vehicle or oleic acid at concentrations of 0, 5, 10, or 25 μg/mL for 24h.

Synovial tissues were obtained from individuals diagnosed with inflammatory polyarthritis undergoing synovectomy or total joint replacement and processed promptly. Fresh synovial tissues were weighed and sliced into thin sections. Single-cell suspensions were prepared by treating with 1 mg/mL collagenase type IV (Worthington, LS004196) and DNase I (100 μg/mL, ZYMO RESEARCH, E1011-A) for 1 hour at 37 °C. Tissue debris was removed using sterile cell strainers (70 μm followed by 40 μm), and $CD4^+$ T cells were isolated using Human CD4 T Cell Isolation kits (BioLegend, #480130 or STEMCELL Technologies).

Fatty acid quantification

Fresh cells or tissues were homogenized, and the free fatty acid (FFA) concentration was measured using the FFA Quantification Kit from Cell Biolabs, Inc. (San Diego, CA), according to the manufacturer's instructions.

LD fractionation and Lipidomics

Lipid droplets (LD) were isolated from activated $CD4^+$ T cells ($\sim 10^8$ cells) using the LD Isolation Kit (Cell Biolabs, MET-5011). After fractionation, the membrane, cytosolic, and LD-enriched fractions were collected for purity assessment. To separate lipids from associated proteins, 1 mL of a chloroform/acetone mixture (1:1, v/v) was added to the LD fraction. Following removal of the organic phase, the remaining pellet was air-dried at room temperature and resuspended in SDS sample buffer for subsequent protein analysis and purity validation.

Lipidomics analysis was performed at the Mayo Clinic Metabolomics Core. LD were extracted with methyl tert-butyl ether (MTBE) and hydrolyzed to release FFAs, which were analyzed by liquid chromatography–tandem mass spectrometry (LC–MS/MS) in negative ion mode. Individual FFAs were identified and quantified using multiple reaction monitoring (MRM) of deprotonated molecular ions, with heptadecanoic acid (C17:0) serving as the internal standard. Fatty acid standards were used to determine absolute concentrations. Samples from healthy and RA LD fractions were adjusted to equal molar amounts of total FFAs. Quantified fatty acids were normalized to the internal standard, expressed as relative percentages of total FFAs, and subsequently transformed into z-scores for comparative representation.

Plasma Membrane fractionation

Healthy and RA $CD4^+$ T cells (1×10^7) were activated with anti-CD3/anti-CD28 Dynabeads for 3 days. Activated healthy $CD4^+$ T cells were then treated with oleic acid at concentrations of 0, 5, 10, or 25 μg/mL for 24h. Following treatment, cells were washed three times with Tris-buffered saline (TBS) and collected by scraping in 1 mL TBS. Cell suspensions were transferred to 50 mL conical tubes and centrifuged to pellet the cells. Membrane and cytosolic fractions were subsequently isolated using the Mem-PER Plus Membrane Protein Extraction Kit (Thermo Fisher Scientific, #89842) according to the manufacturer's instructions. Isolated plasma membrane fractions were subjected to Western blot analysis as indicated.

Acetyl-CoA quantification

The Acetyl-CoA content in the cell-extract was quantified using the Acetyl-CoA Assay Kit (AB87546) (Abcam, MA, USA). The assay was carried out according to the manufacturer's instructions.

Intracellular ATP Quantification

ATP levels were measured using the ATP Determination Kit (Molecular Probes, Thermo Fisher Scientific, Cat. #A22066), luciferin–luciferase bioluminescence reaction based. Activated $CD4^+$ T cells were lysed in the supplied lysis buffer (20 mM Tris, pH 7.5, 0.1 M NaCl, 2 mM EDTA, and 0.01% Triton X-100). A standard curve covering the nano- to micromolar range (10^{-9}-10^{-6}) was prepared. Equal volumes of reaction solution (luciferase, D-luciferin, Mg^{2+}, and reaction buffer) were added to samples and standards in flat 96-well plates, and luminescence was measured immediately using a Promega GloMax Explorer Multimode Microplate Reader. ATP concentrations were determined by interpolating sample luminescence values from the ATP standard curve.

T Cell Transfections

The Human T Cell Nucleofector Kit (Lonza, Catalog #: VPA-1002) was used to overexpress or knockdown specific genes in T cells. Prior to transfection, $CD4^+$ $CD45RA^+$ T cells were stimulated with anti-CD3/anti-CD28-coated beads and cultured for 3 days to ensure appropriate activation. On day two, the T cells were transfected and rested for 24h to recover from the electroporation. On day four, cells were used for molecular and functional analyses.

Real Time PCR

RNA Extraction and RT–PCR. Total RNA was isolated using TRIzol reagent (Molecular Research Center Inc.) and Direct-zol RNA MiniPrep Kits (Genesee Scientific). cDNA was synthesized from total RNA using ribonuclease H reverse transcription (Invitrogen) and oligo(dT) primers. The primer mix has been tested to generate satisfactory qPCR data on the Quant Studio 6 Pro using the following PCR program: Activation: 50 °C for 2 min, Pre-soak: 95 °C for 10 min, Denaturation: 95 °C for 15 sec, Annealing: 60 °C

Please cite this article in press as: Kumar et al., Lipid droplet-induced T cell death sustains autoimmune tissue inflammation, Cell Metabolism (2026), https://doi.org/10.1016/j.cmet.2026.01.014

for 1 min, and Melting curve: 95 °C for 15 sec, 60 °C for 15 sec, 95 °C for 15 sec, performed in triplicate. Expression of individual genes was calculated using a standard curve and normalized to the expression of β-actin. PCR primers used in this study are listed in Table S3.

Flow cytometry

Cell surface staining was performed as previously described.[9,66,67] 4% PFA was used for fixation and 0.1% saponin was used to permeabilize the cells. Samples were analyzed with a CYTEK NL-3000 flow cytometer and data analysis was performed by FlowJo 10.0 (Tree Star). All antibodies used in this study are listed in the above key resources table. To detect intracellular cytokines, single-cell suspensions were stimulated with PMA plus ionomycin in the presence of monensin for 5h before being analyzed by flow cytometry.

Immunofluorescence and confocal microscopy

To visualize intracellular and membrane-integrated proteins, previously published methods were applied.[14,15] Cells were fixed with 4% paraformaldehyde solution (Affymetrix); unless stated otherwise, primary antibodies were incubated at 4°C overnight, followed by a 1h incubation at room temperature with fluorescence-conjugated secondary antibodies. The primary antibodies used were listed in key resources table. Nuclei were stained with 4′,6-diamidino-2-phenylindole (DAPI) (Roche). Images were acquired with a LSM980 system (Carl Zeiss), equipped with a Plan Apochromat 63 3 /1.40-NA oil DICIII objective lens (Carl Zeiss). Data were processed using Carl Zeiss software ZEN (blue) and analyzed by ImageJ software.

Transmission electron microscopy

Cells were resuspended in McDowell's and Trump's fixative for 1 h at room temperature and then pelleted with a microcentrifuge. Cells were washed twice with 0.1 M phosphate buffer for 5 min. Liquid agar was added to the cell pellet and the cells were resuspended, followed immediately by centrifugation. Once the sample had cooled, the agar was removed, and the sample pellet removed with a razor blade and placed into 0.1 M phosphate buffer. After 2 rinses in 0.1 M phosphate buffer, pH 7.2, the sample was placed in 1% osmium tetroxide in the same buffer for 1 h at room temperature. The sample was rinsed twice in distilled water and dehydrated in an ethanolic series, culminating in two changes of 100% acetone. The cell pellet was then placed in a mixture of Spurr resin and acetone (1:1) for 30 min, followed by 2 h in 100% resin with 2 changes. The cell pellet was placed into 100% Spurr resin in an embedding mold and polymerized at 65 °C for ≥12 hr. Ultrathin (70–90 nm) sections were cut on an ultramicrotome with a diamond knife, stained with lead citrate, and examined with a JEOL 1400 transmission electron microscope.

Live cell imaging

Fresh solutions of Hoechst-33342 (2.5μM), (Invitrogen; #H21492) and SYTOX™ Green (1:30,000), (Invitrogen; #S7020) were prepared and added to $CD4^+$ T cells for 30 min prior to the experiment. Images were acquired using the Keyence BZX800E system (Keyence). If needed, ImageJ software was applied to quantify Hoechst-33342 and SYTOX™ Green-positive cells.

Subcellular organelle analysis

Uropod length and numbers were manually quantified in polarized $CD4^+$ T cells based on BODIPY 493/503 staining and cytoskeletal markers. Uropods were defined as rearward cell protrusions positioned opposite the leading-edge nucleus.

Lipid droplets (LD) per cell were counted from BODIPY 493/503-stained confocal images using ImageJ and manually annotated in TEM micrographs. LD size and area were measured using particle analysis tools in ImageJ.

For LD-plasma membrane (PM) spatial analysis, the distance from each LD to the inner face of the PM was measured in TEM images. LD located within 100 nm of the PM were classified as PM-contacting, and the number of such LD per cell was recorded.

Mean fluorescence intensities of PLIN2 and BODIPY were quantified on a per-cell basis using region-of-interest (ROI)–based analysis in ImageJ. Fluorescence thresholds were applied uniformly across all samples and experimental conditions.

For each experimental condition, 50–100 cells were analyzed across three biologically independent replicates. Data were compiled and statistically evaluated using GraphPad Prism 10.0.

Cell Size Analysis

Cells were stained with a plasma membrane specific dye (WGA; AF680) to clearly delineate cell boundaries prior to imaging. Fluorescence images were acquired under identical exposure settings across all conditions. Images were processed using ImageJ/Fiji (NIH, USA). The pixel-to-micrometer scale was calibrated using the microscope's scale bar.

Stained cell perimeters were identified manually using the Freehand Selection Tool following grayscale conversion, thresholding, and binarization. Overlapping cells were separated using the Watershed function. Morphometric measurements including cell area (μm^2), perimeter (μm), and Feret's diameter were obtained using analyze followed by Measure. The equivalent circular diameter (μm) was calculated using the formula:

$$D = 2x\sqrt{\frac{A}{\pi}}$$

Please cite this article in press as: Kumar et al., Lipid droplet-induced T cell death sustains autoimmune tissue inflammation, Cell Metabolism (2026), https://doi.org/10.1016/j.cmet.2026.01.014

Here A is the measured cell area. For each experimental group, at least [n = 30] cells were analyzed, and data were exported into Excel for further statistical analysis.

Histomorphometry of Synovial tissue

The training, validation, and testing set preparation was adapted from the method described by Wang et al.[68] 40x HD H&E-stained images were uploaded and used to quantify cell infiltration in the synovial tissue. (https://lce.biohpc.swmed.edu/maskrcnn/).

Cell membrane leakiness, SYTOX Green Uptake, and lytic cell death

Live-cell imaging was performed using the Keyence Cell Imaging System. Cells were stained with SYTOX Green to detect membrane-compromised (dead or dying) cells and Hoechst-33342 to label all nuclei. For each well, nine fields of view were captured under identical exposure settings. The ratio of SYTOX Green$^+$ to DAPI$^+$ cells was calculated to determine the percentage of dead or dying cells.

Lactate Dehydrogenase Quantification

For the analysis of extracellular lactate dehydrogenase (LDH) activity, both cell culture supernatants and tissue lysates were processed to remove intact cells and debris via centrifugation and filtration.

Cell Culture Supernatant

Conditioned media were collected from cultured cells and centrifuged at 1,000 × g for 5 min at 4°C to pellet residual cells. The clarified supernatant was directly used for LDH quantification.

Tissue Lysates

Single-cell suspensions were obtained by enzymatic digestion of tissue using 1 mg/mL collagenase type IV (Worthington, LS004196) and 100 μg/mL DNase I (ZYMO Research, E1011-A) for 1 hour at 37°C. Tissue debris was removed sequentially using 70 μm and 40 μm sterile cell strainers. Total CD4$^+$ T cells were isolated using human CD4$^+$ T Cell Isolation Kits (BioLegend, #480130 or STEMCELL Technologies). Cell homogenates were centrifuged at 1,000 × g for 10 min at 4°C, and the resulting supernatants were filtered through a 0.2 μm syringe filter to eliminate particulate matter. LDH activity was measured using the CyQUANT LDH Cytotoxicity Assay Kit (Thermo Fisher Scientific) according to the manufacturer's protocol. Data are presented as fold change, calculated as the ratio of LDH activity between experimental and control conditions.

IL-1β Release Assay

Secreted IL-1β was measured in culture supernatants by enzyme-linked immunosorbent assay (ELISA). CD4$^+$ T cells were activated with anti-CD3/anti-CD28 beads (1:3) for 72h. and culture supernatants were collected over the subsequent 24h. IL-1β was quantified using the Human IL-1β ELISA kit (#437004, BioLegend, San Diego) following the manufacturer's instructions.

Extracellular DNA Quantification

Extracellular DNA was quantified from cell culture supernatants collected with and without lipid stress. Supernatants were cleared by centrifugation at 500 × g for 10 minutes to remove cellular debris, transferred to fresh tubes, and kept on ice. Total extracellular double-stranded DNA (dsDNA) was measured using the Qubit dsDNA HS Assay Kit (Thermo Fisher Scientific, Cat# Q32851) according to the manufacturer's protocol. To distinguish nuclear and mitochondrial DNA, supernatants were first digested with proteinase K, followed by phenol–chloroform extraction and ethanol precipitation. Purified DNA was then subjected to PCR using primers targeting nuclear β2-microglobulin (B2M) and the mitochondrial D-loop region. PCR products were analyzed by agarose gel electrophoresis under native conditions.

Quantification of Extracellular LD

Cell-free supernatants were obtained by two-stage centrifugation at 500 × g for 10 minutes, followed by 3,000 × g for 10 minutes. The cleared supernatants were concentrated using Amicon Ultra-4 Centrifugal Filter Units (Millipore Sigma, 10 kDa cutoff) when necessary. Equal volumes of supernatant (10-15 μL) were denatured in Laemmli buffer, resolved by SDS-PAGE, and transferred to nitrocellulose membranes followed by staining with Ponceau S. Membranes were probed with anti-PLIN2 antibodies. Band intensities were quantified using ImageJ and normalized through the Ponceau S stain.

Cell-Free Nuclear DNA and Lipid Droplets in Mouse Plasma

Mouse plasma was collected via cardiac puncture into EDTA-coated tubes and centrifuged at 1,000 × g for 10 minutes at 4 °C to remove cellular components. The supernatant was carefully transferred to fresh tubes and stored at –80 °C until analysis.

Cell-free nuclear DNA (cf-nDNA) was quantified using the Qubit dsDNA HS Assay Kit (Thermo Fisher Scientific, Cat# Q32851) according to the manufacturer's instructions. To confirm nuclear DNA specificity, DNA was extracted from plasma using the QIAamp Circulating Nucleic Acid Kit (Qiagen), and quantitative PCR (qPCR) was performed using primers targeting the β2-microglobulin (B2M) gene. All qPCR reactions were run in technical triplicates.

Plasma lipid droplets (LD) were assessed by PLIN2 immunoblotting. Equal volumes of plasma were denatured in Laemmli sample buffer, resolved by SDS-PAGE, and transferred to nitrocellulose membranes. Membranes were stained with Ponceau S to confirm equal loading, then probed with an anti-PLIN2 antibody (Abcam, Cat# ab108323). Bands were visualized using chemiluminescence, and signal intensity was quantified using ImageJ.

Please cite this article in press as: Kumar et al., Lipid droplet-induced T cell death sustains autoimmune tissue inflammation, Cell Metabolism (2026), https://doi.org/10.1016/j.cmet.2026.01.014

Immunoblotting

Immunoblot analysis of whole cell lysates or subcellular extracts followed previously described protocols.[14] Cells were washed twice with cold phosphate-buffered saline (PBS) and lysed in RIPA buffer (Thermo Fisher Scientific, Cat# 89900) supplemented with Halt protease and phosphatase inhibitor cocktails (Thermo Fisher Scientific). Lysates were incubated on ice for 30 minutes with periodic vertexing, then centrifuged at 14,000 × g for 15 minutes at 4 °C. Supernatants containing total cellular proteins were transferred to fresh tubes. Protein concentration was determined using the BCA Protein Assay Kit (Bio-Rad) according to the manufacturer's instructions. Equal amounts(20-50μg) of protein were mixed with 4× Laemmli sample buffer, boiled at 95 °C for 10 minutes, and resolved by SDS-PAGE using 4–15% or 10–12% polyacrylamide gels. Proteins were transferred to nitrocellulose membranes (Bio-Rad) using a semi-dry blotting system (Bio-Rad Trans-Blot Turbo). Membranes were blocked for 1 hour at room temperature in 5% BSA prepared in TBST (Tris-buffered saline with 0.1% Tween-20), followed by overnight incubation at 4 °C with primary antibodies diluted in blocking buffer. After three washes in TBST, membranes were incubated with HRP-conjugated secondary antibodies for 1 hour at room temperature. Signal detection was performed using ECL reagents (Bio-Rad), and chemiluminescence was captured with a ChemiDoc Imaging System (Bio-Rad).

For plasma immunoblotting, equal sample volumes (10–15μL) were loaded per lane. Ponceau S staining was performed prior to blocking to confirm uniform protein transfer. Densitometric quantification of bands was carried out using ImageJ software, with intensities normalized to total protein loading based on Ponceau S stain.

Immunoprecipitation

For pull-down assays, 500–1000 μg of total protein lysate was incubated with anti-PLIN2 antibody (1:100 dilution, CELL SIGNALING TECHNOLOGY) overnight at 4 °C on a rotator. The next day, Protein A/G magnetic beads (Thermo Fisher Scientific) were added and incubated for 2–3h at 4 °C with continuous rotation. Beads were washed three times with cold lysis buffer and once with PBS to remove non-specifically bound proteins. Immune complexes were eluted by boiling the beads in Laemmli sample buffer at 95 °C for 5–10 minutes. Eluates were resolved by SDS-PAGE and analyzed by immunoblotting as described above. A portion of the input lysate (5–10%) was loaded in parallel as a control. Membranes were probed with anti-zDHHC5 antibody to detect co-immunoprecipitated protein, and GAPDH was used as a loading control for input lysates.

Mass spectrometry analysis

Lipid droplets (LD) were isolated from activated $CD4^+$ T cells using the Lipid Droplet Isolation Kit (Cell Biolabs, Cat# MET-5011). Isolated LD were washed in PBS and subjected to organic extraction using chloroform/acetone (1:1, v/v) to remove lipids. Protein pellets were air-dried and resuspended in 8 M urea in 50 mM ammonium bicarbonate for digestion. Protein concentration was measured using the BCA Protein Assay Kit (Bio-Rad). 50–100 μg of protein per sample was reduced with 10 mM dithiothreitol (DTT), alkylated with 20 mM iodoacetamide, and digested overnight with trypsin (Promega, 1:50 enzyme-to-substrate ratio) at 37 °C. Peptides were desalted using C18 spin columns (Thermo Scientific) and dried under vacuum.

Samples were analyzed by liquid chromatography–tandem mass spectrometry (LC-MS/MS) on a Thermo Scientific Q Exactive Orbitrap mass spectrometer coupled to an EASY-nLC 1200 system. Peptides were separated on a 75 μm × 25 cm C18 column using a 120-minute gradient of 5–35% acetonitrile with 0.1% formic acid. MS1 scans were acquired at a resolution of 70,000, followed by data-dependent MS2 scans at 17,500 resolutions for the top 15 precursors.

Raw data files were analyzed using MaxQuant (v2.6.7.0) with the Andromeda search engine, against the UniProt human reference proteome. Carbamidomethylation of cysteines was set as a fixed modification; oxidation (M) and N-terminal acetylation were considered variable. A 1% false discovery rate (FDR) was applied at the peptide and protein levels. Label-free quantification (LFQ) was enabled.

QUANTIFICATION AND STATISTICAL ANALYSIS

All experiments were conducted independently at least three times, and the resulting data were combined for analysis. No animals or samples that underwent successful procedures or treatments were excluded. Statistical analyses were performed using GraphPad Prism (GraphPad Software). For comparisons between two groups, the Mann–Whitney U test or paired Wilcoxon test was applied when the group size exceeded five. For smaller sample sizes ($\leq$5), and when data met the assumptions of normality and variance, a parametric t-test was used. To correct for multiple comparisons, Hochberg's step-down procedure was applied to control the family-wise error rate at 0.05. For analyses involving three or more groups, one-way ANOVA followed by Tukey's post hoc test and multiple t test were performed. All data points were included in the analysis, and Grubbs' test did not detect any outliers. Results are expressed as mean ± SEM.

For proteomics data, pathway enrichment analyses—such as Gene Ontology (GO) and Kyoto Encyclopedia of Genes and Genomes (KEGG)—were carried out using Enrichr (https://maayanlab.cloud/Enrichr) and Ingenuity Pathway Analysis (IPA, QIAGEN), applying a significance threshold of $P < 0.05$.